SLAYERGEN: A CRYSTAL GENERATIVE MODEL FOR ALL SPACE AND LAYER GROUPS

Anonymous authors
Paper under double-blind review

ABSTRACT

Crystal generative models have shown rapid progress for accelerating the discovery of bulk, periodic materials. However, many material systems such as 2D superconductors, thin film semiconductors, and catalytic surfaces are diperiodic, i.e., aperiodic along one of the lattice directions. These systems are invariant under the *layer groups*, which are known to influence materials properties yet not considered by existing models. In this paper, we propose SLayerGen, a generative model that produces crystals constrained to be invariant to any space or layer group. SLayerGen consists of coarse-to-fine discrete autoregressive lattice generation; transformer-based autoregressive sampling of Wyckoff positions, elements, and numbers of symmetrically unique atoms; and space or layer group equivariant diffusion of atomic coordinates. To facilitate progress in generative modeling of diperiodic materials, we assembled and filtered datasets of monolayers and bilayers, propose relevant evaluation metrics, and developed novel representations for layer group symmetries. For *de novo* generation of diperiodic materials, SLayerGen achieves consistent performance gains over bulk crystal generative models and is competitive when training jointly on bulk and diperiodic materials.

1 INTRODUCTION

Targeted discovery of crystalline materials with functional properties has the potential to drive revolutions in catalysis, computing, energy, and more. Recently, large materials datasets of density functional theory (DFT) calculations (Jain et al., 2013; Schmidt et al., 2024; Levine et al., 2026; Barroso-Luque et al., 2024; Sriram et al., 2025; Allam et al., 2025) have led to a large collection of generative models for bulk periodic inorganic crystals, showing great promise to drastically accelerate materials design (Zeni et al., 2025; Fu et al., 2024b; Kim et al., 2026; Simkus et al., 2025).

However, generative models have not been developed for materials systems containing both periodic and aperiodic dimensions in 3D space. We focus on diperiodic systems, which span thin film interfaces (Gerber et al., 2023; Di Liberto et al., 2022), surfaces (Tran et al., 2016), monolayers (Chakraborty et al., 2021; Haastrup et al., 2018; Gjerding et al., 2021; Zhou et al., 2019; Wang et al., 2019), and multilayer materials (Cao et al., 2018; Castellanos-Gomez et al., 2022; Pakdel et al., 2024). Unlike bulk periodic crystals which are invariant to one of 230 discrete *space groups*, diperiodic crystals are invariant to one of 80 discrete *layer groups* (see Sec. 2 for definitions).

Diperiodic systems offer large surface to mass ratios, frequently yield exotic physics, and are highly tunable via interlayer stacking, twisting, and sliding. Notably, they have been shown to exhibit symmetry-dependent behaviors such as valley-contrasting physics (Schaibley et al., 2016), nonlinear optics (Autere et al., 2018), superconductivity (Saito et al., 2016), and topological properties (Du et al., 2021), offering potential to unlock new paradigms for flexible electronics, quantum computing, and more (Novoselov et al., 2016). The layer group symmetries inherent in these systems have been used to predict bilayer ferroelectrics (Ji et al., 2023), 2D topological materials (Wang et al., 2019), and nodal semimetallic band structures (Wieder & Kane, 2016). We highlight that attributing space groups to diperiodic systems by superficially tiling them along the aperiodic direction is inadequate as 18 of the 80 layer groups do not injectively map to a space group (Fu et al., 2024a).

Despite the promise of diperiodic materials, challenges exist for their data-driven design. Firstly, data is scarce. Atomically thin materials were only discovered in 2004 upon the synthesis of graphene (Novoselov et al., 2004), and the number of experimentally known mono- or few-layer

Reviewers: please read the Reviewer Guidelines (iclr.cc/Conferences/2027/ReviewerGuidelines) and the AI Policy for Reviewers (iclr.cc/Conferences/2027/AIPolicyForReviewers). If you used AI to expand, edit, or polish your review, please provide the input text to the LLM. Better still, consider skipping the LLM and submitting your original text: we, and the authors, are much more interested in your unedited thoughts than in what an LLM has to say. AI-assisted or not, you are putting your name and reputation behind your review: LLM-generated falsehoods, hallucinations or misrepresentations are subject to disciplinary action, which may include desk-rejecting all papers you have authored.

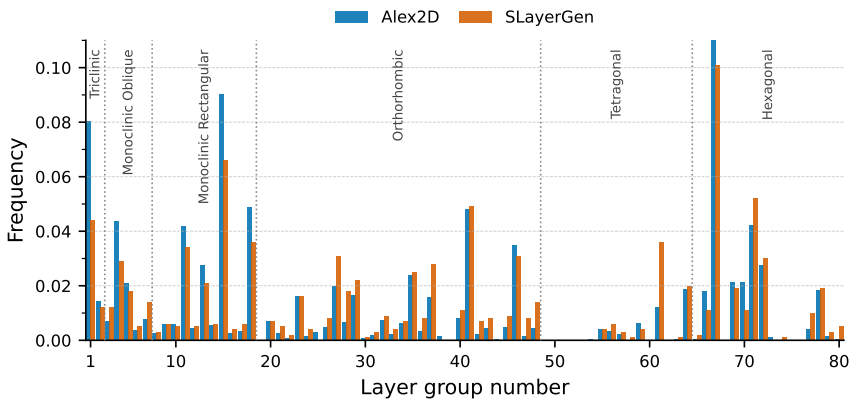


Figure 1: Histograms of occupied layer groups by samples from SLayerGen and by training data from Alexandria (Schmidt et al., 2024; Wang et al., 2023). Layer groups were determined by `spglib` (Fu et al., 2024a; Togo et al., 2024) using a tolerance of 0.01Å. Dashed vertical lines separate layer group numbers by crystal system.

materials is still $\mathcal{O}(10^2)$ (Akhound et al., 2026). Computational predictions slightly raise dataset sizes to $\mathcal{O}(10^3 - 10^4)$ after filtering by loose stability metrics (Zhou et al., 2019; Gjerding et al., 2021; Schmidt et al., 2024). However, dataset construction methods have been limited to elemental substitutions on the few experimentally known structures (Mounet et al., 2018; Zhou et al., 2019; Haastrup et al., 2018), brute-force enumeration through symmetry-derived prototypes (Schmidt et al., 2024; Wang et al., 2023), and exfoliability prediction of known bulk periodic crystals (Zhou et al., 2019; Larsen et al., 2019; Cheon et al., 2017; Gorai et al., 2016). For the latter, we note that bulk crystal datasets are not comprehensive (Davies et al., 2016) and atomically thin materials without bulk analogs have been experimentally observed (Sone et al., 2014; Zhou et al., 2019). Secondly, layer group symmetry strongly influences materials properties and we empirically observed that databases of diperiodic materials contain a large diversity of layer group symmetries (see Figs. 1 and 6). Generative models should thus be capable of reliably reproducing these symmetries. Thirdly, while modeling of periodicity, aperiodicity, continuous translation invariance, and discrete group invariances have been demonstrated across protein, molecular, and bulk crystal generative models (Xu et al., 2022; Jing et al., 2022; Wu et al., 2024; Xie et al., 2022; Chang et al., 2025; Puny et al., 2025), diperiodic materials uniquely require handling all these attributes in a single model. These challenges demand symmetry-aware AI that can expand and intelligently navigate the space of layer group symmetric materials with high data efficiency.

In this paper, we propose a space and layer group-aware generative model (SLayerGen), which enforces constraints and yields invariant likelihoods with respect to any space group or layer group. SLayerGen combines SE(3)-invariant, coarse-to-fine sampling of discretized lattices; permutation-invariant, transformer-based autogressive generation of occupied *Wyckoff positions* (see Sec. 2) and atomic elements; and space or layer group equivariant diffusion of atomic coordinates.

The main contributions of our work are summarized as follows:

- We developed embeddings for layer groups and their Wyckoff positions, corrected two layer group asymmetric unit definitions from the International Tables of Crystallography, and enumerated symmetrically unique regions of every Wyckoff position to build uniform priors over symmetrically unique atom positions.
- By leveraging components from both bulk crystalline and molecular models, we built a generative model which, in addition to modeling space group symmetries, explicitly models layer groups. We also corrected an inconsistency between training and model constraints from a prior work when training diffusion models on hexagonal groups.
- We curated datasets of monolayers and bilayers to benchmark *de novo* generation of diperiodic materials while proposing several evaluation metrics.
- We demonstrate state-of-the-art results and competitive performance when jointly training on triperiodic and diperiodic materials.

2 PRELIMINARIES

Space groups and layer groups All crystals with d periodic dimensions are invariant with respect to at least one crystallographic group $G^d \in \mathbb{G}^d$. A crystallographic group G^d is comprised of an infinite subgroup of discrete lattice translations $T_L^d = \{n_1 L_1, ..., n_d L_d | n_i \in \mathbb{Z}, L_i \in \mathbb{R}^3\}$ and a set of group elements with action $g^d(\cdot) = R_{g^d}(\cdot) + v_{g^d}$ where $R_{g^d} \in \mathrm{O}(3)$ and $v_{g^d} \in \mathbb{R}^3$ is a non-lattice translation. For $d = 3$, there are 230 crystallographic *space groups*. For $d = 2$, there are 80 crystallographic *layer groups*, generalizing the 17 commonly known wallpaper groups. In the conventional unit cell bases of the layer groups where the center of mass along the L_3 axis is set to zero, $v^z_{g^2} = 0$ and R_{g^2} is block diagonal with $R_{g^2} = R^{xy}_{g^2} \bigoplus R^z_{g^2}$ where $R^{xy}_{g^2} \in O(2)$ and $R^z_{g^2} \in O(1)$ (Fu et al., 2024a). For simplicity, we will drop d from the notation going forward and assume equations apply to both $d = 2$ and 3 unless stated otherwise.

Unit cells Redundancy from lattice translations T_L can be removed from crystal representation via three basis vectors, $L = [L_1, L_2, L_3] \in \mathbb{R}^{3\times3}$, which define a parallelepiped $\Gamma \in \mathbb{R}^3$ called the unit cell. A crystal M with N atoms per unit cell can be described by the tuple $M = (A, X, L)$, where $A = (a'_1, ..., a'_N) \in \mathbb{A}^N$ are the discrete atomic elements, $X = (Lx'_1, ..., Lx'_N) \in \mathbb{R}^{3\times N}$ are the Cartesian atom coordinates, and $\{x'_1, ..., x'_N | x'_i \in \Gamma\}$ are the *fractional* atom coordinates. For bulk crystals with space group symmetry, the unit cell is finite and the infinitely periodic crystal can be reconstructed from it as $\{(a'_i, x'_i + n_1 e_1 + n_2 e_2 + n_3 e_3)^N_{i=1} | n_i \in \mathbb{Z}\}$ where $e_i \in \mathbb{R}^3$ is from the standard basis. In contrast, crystals with layer group symmetry are reconstructed as $\{(a'_i, x'_i + n_1 e_1 + n_2 e_2)^N_{i=1} | n_i \in \mathbb{Z}\}$ and the unit cell is unbounded along L_3. Here, L_3 merely serves to provide a basis vector for defining atomic coordinates and group representations. In our model, we described atom positions using fractional coordinates for periodic dimensions and Angstrom distances along L_3 for aperiodic dimensions. We will refer to the latter as "aperiodic fractional coordinates". We canonicalized the non-unique choice of unit cell with the *conventional unit cell* (Aroyo et al., 2016) which contains all the symmetries of the crystallographic group.

Wyckoff positions Given a crystallographic group and a point $x \in \mathbb{R}^3$, the *stabilizer* group $G_x \equiv \{g | gx = x\} \subset G$ is the finite subgroup of G that leaves x invariant. A Wyckoff position is the set of points with conjugate stabilizer groups, i.e., $\{x' | \exists\, g \in G : G_{x'} = g G_x g^{-1}\}$. There are 1731 Wyckoff positions across the 230 space groups and 477 Wyckoff positions across the 80 layer groups. When a Wyckoff position's stabilizer group only contains the identity, it is called the *general Wyckoff position* and consists of the interior of the asymmetric unit. When a Wyckoff position's stabilizer group contains nontrivial group elements, it is called a *special Wyckoff position* and either consists of a point (e.g., at an inversion center), set of line segments (e.g., rotation axes), or facets (mirror planes) on the ASU boundaries. The *orbit* size of each Wyckoff position (modulo lattice translations) is called the Wyckoff multiplicity and defined as $|\{gx | g \in G, gx \in \Gamma\}|$.

Asymmetric units To enable memory-efficient lazy data loading and construct uniform priors over atom positions that are inequivalent under actions of crystallographic groups, we removed redundancy induced by the crystallographic group $G \supseteq T_L$ by storing crystals in terms of their *asymmetric unit* (ASU) $\Pi \in \mathbb{R}^3$. In this representation, a crystal is described as fractional coordinates $X = \{(x_1, ..., x_n) | x_i \in \Pi\} \in \mathbb{R}^{3\times n}$, atomic elements $A = (a_1, ..., a_n) \in \mathbb{A}^n$, and Wyckoff positions $W = \{(w_1, ..., w_n) | w_i = G_{x_i}\} \in \mathbb{W}^n$ where $n \leq N$. The infinitely periodic crystal can be reconstructed from the asymmetric unit as $\{(a_i, g_{ij} x_i) \mid x_i \in \Pi,\ g_{ij} \in G/w_i,\ i \in (1, ..., n)\}$. We canonicalized the non-unique choice of ASU using those in the International Tables for Crystallography (Aroyo et al., 2016). To ensure that the ASU is *exact*, i.e., tiles $\mathbb{R}^3$ without overlaps at boundaries, we additionally defined which ASU faces, edges, and vertices are (partially) open or closed (see Sec. 4.1).

Crystallographic group equivariant neural networks Given a group of isometries G', Rezende et al. (2019) and Köhler et al. (2020) showed that transforming a G'-invariant probability density according to a G'-equivariant flow will preserve invariance. Yarotsky (2022) and Puny et al. (2022) then showed how to symmetrize neural networks to be invariant or equivariant via group averaging without reducing expressivity of the original model. Symmetrization was later used to build space group equivariant functions $f : \mathbb{R}^3 \to \mathbb{R}^3$ for bulk crystals and metamaterials (Chang et al., 2025; Puny et al., 2025; Mirramezani et al., 2025) given a T_L-invariant neural network $\hat{f} : \mathbb{R}^3 \to \mathbb{R}^3$ using

the following operator:

$$f(x) = \frac{1}{|G/T_L|} \sum_{g \in G/T_L} R_g^{-1} \hat{f}(gx). \tag{1}$$

Eq. 1 has been proven to satisfy equivariance, i.e., $f(gx) = R_g f(x)$. We use the same operation to symmetrize a denoising score network to be equivariant with respect to any space or layer group.

Chang et al. (2025) and Puny et al. (2025) also showed that transforming atom positions according to a space group equivariant flow preserves the stabilizer group (i.e., Wyckoff position) of the atoms. Specifically, the following holds for arbitrary scalar $\epsilon \in \mathbb{R}$ and stabilizer group element $g_x \in G_x$:

$$g_x(x + \epsilon f(x)) = x + \epsilon f(x) \implies G_x \subseteq G_{x+\epsilon f(x)}. \tag{2}$$

3 Related Work

Protein folding and molecular generation Early generative models for molecules focused on discrete string representations (Gómez-Bombarelli et al., 2018), later generating all-atom 3D geometries autoregressively (Gebauer et al., 2020) and with E(3)-equivariant diffusion models (Shi et al., 2021; Xu et al., 2022; Hoogeboom et al., 2022). Others diffused relative atom orientations, e.g., via periodic torsion angles (Jing et al., 2022; Wu et al., 2024). Similarly to molecules and proteins, diperiodic materials require generation of periodic and continuously translation invariant aperiodic coordinates. However, diperiodic materials also have invariances to non-translational discrete isometries.

Generative models for bulk materials In the last few years, a large body of generative models have been developed for bulk crystalline materials, including variational autoencoders (VAE) (Ren et al., 2022; Hoffmann et al., 2019), generative adversarial networks (Kim et al., 2020), diffusion models (Xie et al., 2022; Jiao et al., 2023; Zeni et al., 2025; Lin et al., 2024; Yang et al., 2024b; Joshi et al., 2025), flow matching models (Miller et al., 2024), stochastic interpolants (Höllmer et al., 2025), Bayesian Flow Networks (Wu et al., 2025), and fine-tuned large language models (Sriram et al., 2024; Yang et al., 2024a; Park et al., 2025; Gruver et al., 2024; Yan et al., 2024).

Several models exist which enforce space group constraints during generation. Some of these models focused on generation of discrete space groups and Wyckoff positions (Zhu et al., 2024; Mistal et al., 2023; Jiao et al., 2024; Cao et al., 2024; Kazeev et al., 2024; Kelvinius et al., 2025), while others focused on constrained generation of atom coordinates using P1-invariant models and projections onto Wyckoff positions (Jiao et al., 2024; Levy et al., 2025; Ruple et al., 2025). Recently, SGEquiDiff (Chang et al., 2025) and SGFM (Puny et al., 2025) constructed space group invariant model likelihoods and achieved state-of-the-art performance by symmetrizing diffusion and flow matching models with space group equivariance, automatically preserving space group symmetries at every step. SLayerGen builds on the work of SGEquiDiff to enable layer group constrained generative modeling for the first time while preserving the ability to model space groups.

Data-driven prediction of diperiodic materials Besides the aforementioned methods for diperiodic materials dataset construction (Sec. 1), several data-driven approaches have been applied to diperiodic materials design. Some works trained crystal diffusion models that spuriously assume diperiodic materials have triperiodicity (Lyngby & K.S., 2022; Gao et al., 2025; Xu et al., 2025). Another work (Dong et al., 2023) predicted elemental compositions with a transformer, selected structural prototypes from known diperiodic materials, and relaxed atom positions with a machine learning interatomic potential (MLIP) (Dong et al., 2023). Unlike these approaches, SLayerGen models the layer group symmetries of diperiodic materials and the space group symmetries of bulk materials while generating entire atomic structures from scratch.

4 SLayerGen

4.1 Crystal representation and generation process

We represented each crystal as a tuple $M = (G, L, A, W, X) \in (\mathbb{G}, \mathbb{R}^{3\times3}, \mathbb{A}^n, \mathbb{W}^n, \mathbb{R}^{n\times3})$, where n is the number of atoms in the exact asymmetric unit, $G \in \mathbb{G}$ is the space or layer group, $L \in \mathbb{R}^{3\times3}$ is

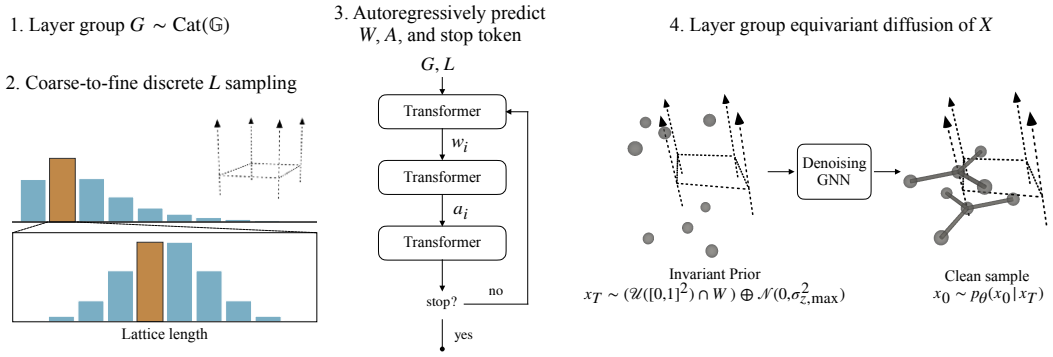


Figure 2: Illustration of our diperiodic crystal generation process.

the conventional lattice basis, $A \in \mathbb{A}^n$ are elements, $W \in \mathbb{W}^n$ are Wyckoff positions, and $X \in \mathbb{R}^{n\times 3}$ are fractional atom coordinates. To handle directional dependencies from symmetry constraints, we factorized generation as follows:

$$p(M) = p(G) \times p(L|G) \times p(W, A|L, G) \times p(X|W, A, L, G). \tag{3}$$

To reduce memory requirements and enable atom diffusion from uniform priors over symmetrically inequivalent atom positions, we removed redundancy from each Wyckoff position by finding its intersection with the corresponding exact ASU. We refer to these intersections as *Wyckoff shapes* as they consisted of points, lines, line segments, planes, polygons, and interiors of the ASUs. For the space groups, we used the intersections enumerated by SGEquiDiff (Chang et al., 2025) which leveraged exact ASU boundary conditions found by Grosse-Kunstleve et al. (2011). However, exact ASUs for the layer groups have not been enumerated to the best of our knowledge, so we removed redundancy from every layer group Wyckoff position ourselves using custom visualization and validation scripts (see Sec. 7.8 for details). During this process, we found and corrected erroneous entries in the inexact asymmetric units listed for layer groups 7 and 46 in the International Tables of Crystallography (Litvin & Kopský, 2010).

We set $p(G)$ to the empirical training distribution. Now we discuss the remaining distributions.

4.2 Coarse-to-fine discrete sampling of L

Most crystallographic groups impose constraints on the crystal lattice lengths ($a = ||L_1||_2, b = ||L_2||_2, c = ||L_3||_2$) and angles ($\alpha = \angle L_2L_3, \beta = \angle L_1L_3, \gamma = \angle L_1L_2$) (see Sec. 7.7). To enforce these constraints during lattice generation in SLayerGen, we extended the lattice generation model of SGEquiDiff (Chang et al., 2025) to support layer group constraints and to mask out generation of the superficial lattice length c. While DiffCSP++ (Jiao et al., 2024) also proposed a masked diffusion approach for constraining lattice parameters, it does not enforce positive determinant in the lattice matrix and thus is not guaranteed to preserve the 22 chiral space groups with enantiomorphic pairs (Aroyo et al., 2016). Briefly, our model achieves efficient high-resolution and constrained lattice generation via coarse-to-fine autoregressive sampling of discretized lattice parameters where crystallographic group constraints are enforced at training and inference time via logit masking. The model likelihoods are modeled as follows:

$$p(L|G) = \prod_{i=1}^{6} p(l_i|l_{<i}, G) \qquad p(l_i|l_{<i}, G) = \prod_{k=1}^{K} p(b_k|b_{k-1}, l_{<i}, G)$$

where $l_i \in \mathbb{R}$ is a lattice parameter, K is the number of resolutions, and b_k is a class from the categorical distribution at resolution k with n_l categories. We trained an MLP with the cross-entropy loss with $K = 2$ and $n_l = 100$. Lattice parameters were modeled as the sequence, (a, b, c, α, β, γ), and we maximized likelihoods of ground truth parameters conditioned on preceding lattice lengths and angles noised with uniform random noise with 0.3Å and 5° ranges, respectively.

4.3 Transformer-based autoregressive sampling of W, A, and n

We used a transformer based on SGEquiDiff (Chang et al., 2025) to autoregressively generate Wyckoff positions and elements. A learnable stop token was used to implicitly learn the number of atoms per

material. Sequences of Wyckoff positions and elements were ordered lexicographically and logits of Wyckoff positions consisting of 0D points were masked if atoms were already generated there. The following factorized model likelihood was trained with a cross-entropy loss:

$$p(W, A|L, G) = \prod_{i=1}^{n} \Big[p(w_i|w_{<i}, a_{<i}, L, G) p(a_i|w_{\leq i}, a_{<i}, L, G) p(\text{stop}|w_{\leq i}, a_{\leq i}, L, G) \Big]. \quad (4)$$

To extend SGEquiDiff (Chang et al., 2025) for layer groups and encourage learning correlations across different groups, we created embeddings of layer groups and their Wyckoff positions consistently with SGEquiDiff's embeddings for space groups and their Wyckoff positions. These embeddings were used to encode intermediate states and keys in the transformer. See Sec. 7.8.1 for details.

4.4 Space and layer group equivariant diffusion of X

We generated atomic fractional coordinates with noise conditional score matching diffusion (Song & Ermon, 2019). Similarly to SGEquiDiff (Chang et al., 2025), we learned scores with a G-invariant "group wrapped normal" (GWN):

$$p(x_t|x_0) \propto \sum_{g \in G} \exp\Big(-\frac{1}{2}(x_t - gx_0)^T \Sigma_t^{-1} (x_t - gx_0) \Big) \quad (5)$$

where x_t is a noisy sample, x_0 is a clean sample, and Σ_t is the noise covariance matrix at time t. We made several changes compared to SGEquiDiff. First, since layer groups are invariant with respect to continuous global translations along the aperiodic direction, we followed work on molecular and particle systems (Xu et al., 2022; Köhler et al., 2020) to build *center of mass (CoM)-free distributions*; we always translated the mean z-coordinate of our diperiodic materials to zero, including rigidly aligning the z-component of the CoM between clean and noised diperiodic structures before score computation. Second, when G is a layer group and the noise scale Σ_t increases, the distribution does not approach uniform in the aperiodic direction as it does in the periodic directions. To handle this, we chose diagonal but anisotropic noise covariance $\Sigma_t = \sigma_{t,xy}^2 I_2 \bigoplus \sigma_{t,z}^2 I_1$ where $\sigma_{t,xy}, \sigma_{t,z} \in \mathbb{R}$, $I_d \in \mathbb{R}^{d \times d}$ is the identity, and $\sigma_{t,z}$ describes the noise on aperiodic coordinates in Angstroms. Using variance exploding noise schedules, we note that the resulting noise prior, uniform in the periodic plane ($\mathcal{U}([0,1]^2)$) and Gaussian along the L_3-axis ($\mathcal{N}(0, \sigma_{T,z}^2)$), is trivially invariant to all layer groups. Third, Chang et al. (2025) proved that the score of a GWN with isotropic noise is equivariant, i.e., $\nabla_{x_t} \log p(gx_t|x_0) = R_g \nabla_{x_t} \log p(x_t|x_0)$, and thus preserves invariant distributions (Köhler et al., 2020) and stabilizer groups via Eq. 2. We prove equivariance also holds for layer groups with our choice of Σ_t in Sec. 7.9.

The equivariance proof by Chang et al. (2025) requires that the matrix representation R_g, where $g = \{R_g, v_g\} \in G$, is orthogonal; however, while R_g is always orthogonal in real space, it is not orthogonal *in fractional coordinates* for hexagonal groups, as noted by Puny et al. (2025). We verified empirically that ignoring the non-orthogonality results in non-equivariant GWN scores in fractional coordinates, yielding a mismatch between target scores and predictions from models symmetrized by Eq. 1. To resolve this issue, we computed scores of hexagonal groups in a dimensionless Cartesian basis and then converted the scores back to fractional coordinates. In Sec. 7.9, we describe the induced score function $\phi(x_t|x_0)$ in fractional coordinates and prove that it satisfies equivariance, i.e., $\phi(gx_t|x_0) = R_g \phi(x_t|x_0)$.

We learned the scores of Eq. 5 by reconstructing the conventional unit cell from its asymmetric unit and symmetrizing a denoising graph neural network using Eq. 1. Plane waves and random Fourier features were used to embed periodic and aperiodic coordinates, respectively. See Sec. 7.11.2 and 7.10 for further details on the diffusion model architecture, training, and inference.

5 Experiments

Datasets Since only a few hundred diperiodic materials have been experimentally cataloged (Akhound et al., 2026), we evaluated SLayerGen on four DFT-based datasets of diperiodic materials: 2DMatPedia (Zhou et al., 2019), C2DB (Haastrup et al., 2018), BiDB (Pakdel et al., 2024), and Alex2D (Schmidt et al., 2024; Wang et al., 2023). 2DMatPedia was constructed by screening all

Table 1: Results on the 2DMatPedia dataset. Best value per metric is bold, second best is underlined. Mean and standard deviations are computed by training models independently over 3 seeds.

	Time ↓ (s / batch)	Validity (%) ↑ Structure	Validity (%) ↑ Composition	U.N. rate (%) ↑ Structure	U.N. rate (%) ↑ Template	Distribution distance ↓ $W_{\text{Thickness}}$	Distribution distance ↓ W_ρ	Distribution distance ↓ $W_{N_{el}}$	Distribution distance ↓ JSD_G	Stable (%) ↑ E_{hull}	Stable (%) ↑ $E_{\text{hull}}\Gamma$	S.U.N. (%) ↑ Structure	S.U.N. (%) ↑ Template
DiffCSP	212	94.9	**82.3**	98.2	9.4	1.054	0.052	3.373	0.762	17.5	11.7	10.6	2.4
DiffCSP++	247	96.0	73.4	91.7	6.3	**0.515**	0.032	1.039	0.180	36.7	26.8	19.9	3.9
MatterGen	1555	**99.0**	78.6	**98.8**	9.8	5.118	**0.036**	1.858	0.701	41.5	**33.2**	**30.7**	4.2
SLayerGen3D	157 ± 8	93.4 ± 1.0	71.7 ± 0.3	91.8 ± 0.8	27.3 ± 1.8	2.005 ± 0.210	0.063 ± 0.005	$\mathbf{0.185 \pm 0.058}$	0.208 ± 0.011	36.5 ± 1.0	29.4 ± 1.5	21.3 ± 1.3	4.7 ± 0.9
SLayerGen	$\mathbf{139 \pm 5}$	98.4 ± 0.4	70.8 ± 0.4	90.9 ± 1.6	$\mathbf{30.3 \pm 0.9}$	1.167 ± 0.007	0.052 ± 0.007	0.195 ± 0.013	$\mathbf{0.200 \pm 0.008}$	$\mathbf{42.8 \pm 1.8}$	$\mathbf{33.2 \pm 0.4}$	24.5 ± 0.9	$\mathbf{5.8 \pm 0.4}$
SLayerGen ($T_{G,W} = 2.0$)	**136**	96.8	68.1	94.1	**48.0**	1.040	0.044	0.255	**0.319**	37.7	26.5	21.5	**7.0**

Table 2: Results on the C2DB dataset. Best value per metric is bold, second best is underlined.

	Time ↓ (s / batch)	Validity (%) ↑ Structure	Validity (%) ↑ Composition	U.N. rate (%) ↑ Structure	U.N. rate (%) ↑ Template	Distribution distance ↓ $W_{\text{Thickness}}$	Distribution distance ↓ W_ρ	Distribution distance ↓ $W_{N_{el}}$	Distribution distance ↓ JSD_G	Stable (%) ↑ E_{hull}	Stable (%) ↑ $E_{\text{hull}}\Gamma$	S.U.N. (%) ↑ Structure	S.U.N. (%) ↑ Template
DiffCSP	126	99.2	82.6	89.0	13.0	0.265	**0.022**	1.313	0.617	52.7	49.4	35.5	4.3
DiffCSP++	141	99.6	83.4	78.1	5.0	**0.235**	0.018	0.302	0.138	61.0	54.4	35.8	4.4
MatterGen	1308	**99.7**	80.2	**94.3**	10.1	0.508	0.045	0.648	0.521	59.3	**54.3**	**45.2**	5.0
SGEquiDiff	82	96.7	83.2	80.5	17.5	1.669	0.012	0.097	0.284	49.0	42.3	23.9	3.0
SLayerGen3D	94	99.0	83.2	68.7	17.1	0.518	0.031	0.117	0.169	65.0	58.7	29.4	5.2
SLayerGen	**81**	**99.7**	**84.4**	76.5	**19.9**	0.604	0.037	0.173	**0.183**	**60.0**	54.1	33.0	**5.6**
SLayerGen ($T_{G,W} = 2.0$)	86	99.2	81.0	83.6	**38.4**	0.791	0.050	**0.069**	**0.239**	54.3	46.7	30.0	**6.8**

layered bulk materials (including hypothetical ones) from the Materials Project (Jain et al., 2013), theoretically exfoliating them into monolayers, and substituting their elements. C2DB conducted elemental substitutions only in experimentally known monolayers. BiDB extracted stable monolayers from C2DB with up to 10 atoms per unit cell and stacked them in various configurations to create homobilayers. Alex2D enumerated hypothetical prototypes of layer groups and Wyckoff positions and then occupied them with elements that satisfy charge neutrality. We note that merging datasets is nontrivial as each one uses distinct DFT settings (see Sec. 7.13). We filtered materials from each dataset that are unlikely to be synthesizable, as described in Sec. 7.1.

After data filtering, we constructed 70/15/15 data splits from the remaining 2,696 of 6,351 monolayers from 2DMatPedia, 8,502 of 16,905 monolayers from C2DB, 2,641 of 11,184 bilayers from BiDB, and 30,082 of 137,833 materials from Alex2D. We standardized all data and generated structures, superficially represented as having bounded unit cells, by padding the "lattice length" in the aperiodic direction to 25Å plus the max empirical layer thickness and then centering the mean of each layer to $z = 0.5$ (see Sec. 7.13.1). Layer groups and Wyckoff positions were determined with `spglib.get_layergroup` using `symprec=0.01` for data pre-processing and `symprec=0.1` for model evaluation (Togo et al., 2024; Fu et al., 2024a).

To assess whether SLayerGen's ability to handle layer groups harms its performance on space group symmetric materials, we also provide results on the MP20 dataset (Xie et al., 2022), containing 45,231 experimentally observed triperiodic crystals with up to 20 atoms per unit cell.

Baselines DiffCSP (12.3M parameters) (Jiao et al., 2023) enforces P1 space group symmetry and jointly diffuses elements, lattice matrices, and fractional atom coordinates. The model uses a P1-invariant GNN with fully-connected graphs under periodicity. MatterGen (44.6M parameters) (Zeni et al., 2025) similarly enforces P1 space groups and does joint diffusion, but leverages Cartesian coordinates and an SE(3)-equivariant GNN with radius-based graphs. DiffCSP++ (Jiao et al., 2024) enforces constraints from larger space groups with per-step projections during diffusion given templates from training data. SGEquiDiff (5.5M parameters) (Chang et al., 2025) also enforces space group constraints but builds crystals from scratch by combining autoregressive sampling of lattices, Wyckoff positions, and elements with space group equivariant diffusion of atom coordinates. We note that DiffCSP, DiffCSP++, and MatterGen do not learn the distribution over number of atoms per unit cell and DiffCSP++ does not learn the distribution over occupied Wyckoff positions, instead relying on examples from training data.

To isolate the effect of enforcing layer group symmetries from model architecture, training recipe, and other hyperparameters, we also compared to *SLayerGen3D*, which is identical to SLayerGen (6.0M parameters) but trains on diperiodic materials represented as having space group symmetries.

Metrics Each generative model was evaluated on a budget of 10,000 generated materials. We computed average sampling times per batch of 500 materials on a single A40 NVIDIA GPU, structural validity defined by all atomic nearest neighbor distances being between 0.5Å and 7.5Å, and compositional validity based on `SMACT` (Davies et al., 2016). We note that roughly 10% of known crystals fail the compositional validity checker (Xie et al., 2022). Of 1000 structurally and

Table 3: Results on the BiDB dataset. Best result is bold, second best is underlined.

	Time ↓	Validity (%) ↑		U.N. rate (%) ↑		Distribution distance ↓					Stable (%) ↑		S.U.N. (%) ↑	
	(s / batch)	Structure	Composition	Structure	Template	$W_{\text{Thickness}}$	$W_{d_{\text{Interlayer}}}$	W_ρ	$W_{N_{\text{el}}}$	JSD_G	B	BΓ	Structure	Template
DiffCSP	158	**99.6**	79.9	**96.8**	10.6	0.188	0.036	0.312	2.050	0.597	80.0	62.8	**63.6**	4.7
DiffCSP++	221	97.3	83.3	80.1	2.2	0.298	**0.067**	**0.045**	0.675	**0.121**	90.0	73.4	56.8	5.5
MatterGen	1896	**99.6**	82.0	79.4	8.9	0.324	0.043	0.483	0.655	0.411	91.0	80.6	51.2	5.0
SLayerGen3D	**116**	98.7	82.4	60.2	15.6	0.822	0.212	0.0.046	0.310	0.182	**92.8**	**79.4**	41.6	9.0
SLayerGen	131	97.8	**86.1**	50.3	10.9	**0.061**	0.044	0.638	**0.188**	0.178	93.2	80.2	36.2	**7.6**
SLayerGen ($T_{G,W} = 2.0$)	164	95.9	80.4	60.6	**22.5**	0.160	0.085	0.998	**0.209**	0.268	**93.5**	73.4	37.2	**11.3**

Table 4: Results on the Alex2D dataset. Best result is bold, second best is underlined.

	Time ↓	Validity (%) ↑		U.N. rate (%) ↑		Distribution distance ↓				Stable (%) ↑		S.U.N. (%) ↑	
	(s / batch)	Structure	Composition	Structure	Template	$W_{\text{Thickness}}$	W_ρ	$W_{N_{\text{el}}}$	JSD_G	E_{hull}	$\text{E}_{\text{hull}}\Gamma$	Structure	Template
DiffCSP	125	99.1	72.7	**87.8**	7.3	**0.130**	0.015	1.072	0.614	59.7	52.9	45.1	2.5
DiffCSP++	137	**99.9**	75.8	73.6	1.8	0.161	0.012	0.236	0.108	75.0	61.6	37.1	1.3
MatterGen	973	99.6	74.5	**85.7**	6.9	0.209	0.019	0.302	0.451	79.7	**70.9**	**49.9**	3.9
SLayerGen3D	91	99.5	76.0	68.4	7.5	0.262	0.007	0.080	0.124	76.9	65.1	35.9	2.0
SLayerGen	78	**99.9**	**76.9**	70.7	7.5	0.143	**0.010**	0.148	**0.149**	75.4	63.9	34.2	2.1
SLayerGen ($T_{G,W} = 2.0$)	79	99.5	71.0	80.6	**20.0**	0.253	0.021	0.192	**0.212**	65.8	52.6	32.3	**4.4**
SLayerGen (Alex2D + MP20)	78	**100.0**	**76.8**	66.1	7.4	0.145	**0.011**	**0.093**	**0.131**	**80.6**	68.8	36.9	2.2

Table 5: Results on the MP20 dataset of bulk triperiodic crystals.

	Time ↓	Validity (%) ↑		U.N. rate (%) ↑		Distribution distance ↓			Stable (%) ↑		S.U.N. (%) ↑	
	(s / batch)	Structure	Composition	Structure	Template	W_ρ	$W_{N_{\text{el}}}$	JSD_G	E_{hull}	$\text{E}_{\text{hull}}\Gamma$	Structure	Template
SGEquiDiff	**285**	99.8	86.2	81.9	16.7	**0.131**	0.159	0.150	75.4	65.0	48.0	5.6
SLayerGen3D	318	99.8	85.2	82.4	17.9	0.204	**0.124**	0.151	**76.7**	**65.1**	46.6	6.0
SLayerGen (Alex2D + MP20)	331	99.8	84.4	**89.5**	**24.9**	0.297	0.188	0.153	69.0	59.4	**48.4**	**7.8**

compositionally valid random samples, we measured goodness-of-fit via distributional distances to the test set: Jensen-Shannon divergences (JSD) for the layer groups G and the 18 layer groups which don't map injectively to a space group G_{18}, Wasserstein distances for areal densities projected along the lattice plane ρ (μg/cm^2), monolayer thicknesses (Å), bilayer interlayer distances (Å), and numbers of unique elements per structure N_{el}. We then computed uniqueness and novelty (U.N.) rates with two methods. First, we measured U.N. *Structure* rates with respect to the training set using `pymatgen StructureMatcher` (Ong et al., 2013) (`ltol=0.2`, `stol=0.3`, and `angle_tol=5`), which applies affine lattice transformations to match atomic structures within user tolerances. Second, following SymmCD (Levy et al., 2025), we computed chemistry-agnostic U.N. *template* rates, where a template was defined as the multiset of a structure's layer group and occupied Wyckoff positions.

To assess the ability of generative models to find new realistic structures, we conducted relaxations on 1,000 valid structures per model using `Orb-v3` (Rhodes et al., 2025); we then measured stability and recomputed uniqueness and novelty based on the relaxed structures. For the BiDB dataset, we used `orb_v3_conservative_inf_omat` with BJ-dampled D3 corrections. Stability was defined as the relaxed bilayer having lower total energy than its individual relaxed monolayers (B) and having dynamically stable Γ-point phonons. For all other datasets, we used `orb_v3_conservative_inf_mpa` and defined stability as having (1) an energy above the hull E_{hull} less than 200 meV/atom with respect to the Materials Project `v2023.02.07` and (2) dynamically stable Γ-point phonons. We report stability rates with and without the phonon constraint as well as the rate of S.U.N. structures and templates, where we introduce the S.U.N. template rate to assess how often a stable structure with a unique and novel template is generated. This metric aims to measure generalization beyond traditional elemental substitutions in known structures.

MLIP-based relaxations were conducted with a force convergence tolerance of 0.005 eV/Å using the fast inertial relaxation engine (Bitzek et al., 2006). To prevent spurious interactions between periodic images along the aperiodic direction, we padded the lattice c-axis to 25Å of vacuum and fixed it during relaxation. Before computing uniqueness or novelty of structures, they were all padded to the same c-axis length as `StructureMatcher` is sensitive to variable lengths.

Results On the 2DMatPedia, C2DB, and Alex2D datasets, SLayerGen achieved the best JSD metric for layer groups, including compared to space group constrained models (Tables 1-4). While DiffCSP++ beat SLayerGen's layer group JSD metric on the BiDB dataset, we attribute the difference to DiffCSP++ leveraging ground truth combinations of Wyckoff positions from training data. In Fig. 5, we show histograms of the layer groups of structures generated by MatterGen, DiffCSP++, and SLayerGen after training on Alex2D. The distributions reveal that MatterGen heavily oversamples P1 crystals (potentially explaining its inflated (S.)U.N. structure rates since P1 groups impose the fewest constraints on atom positions) and DiffCSP++ cannot sample many monoclinic or orthorhombic layer groups, while SLayerGen closely reproduces the training distribution of layer groups.

Significantly, SLayerGen also achieved the highest S.U.N. template rate on 3 of 4 datasets with the fastest or second fastest generation speed, highlighting SLayerGen's ability to generalize to unseen structure templates. We show examples of SLayerGen-generated diperiodic materials with S.U.N. templates in Fig. 3. While MatterGen had a higher S.U.N. template rate than the default SLayerGen configuration on the Alex2D dataset, SLayerGen's modular architecture permits selective inference-time tempering. We leveraged this capability to temper the distributions over layer groups and Wyckoff positions (SLayerGen $T_{G,W} = 2.0$), leading to the highest S.U.N. template rate at the cost of slightly lower stability and S.U.N. structure rates (Table 4). SLayerGen also achieved the best performance in generating the correct layer group distributions over the 18 layer groups that do not map injectively to a space group (Table 8). This is significant because, for example layer group 4 is polar in-plane and layer group 11 is polar out-of-plane, while both share the space group 6 (Fu et al., 2024a).

By comparing SLayerGen to SLayerGen3D, we found that modeling diperiodic materials with layer groups instead of space groups enhanced performance across several metrics. In particular, on 3 of the 4 datasets, SLayerGen achieved higher S.U.N. rates, better validity rates, and distributional distances for thickness.

Since SLayerGen can condition on any space or layer group, we evaluated the model's ability to train on both di- and triperiodic crystals. On most metrics for C2DB and MP20, SLayerGen3D performed comparably or slightly better than SGEquiDiff, the baseline model upon which SLayerGen is most closely related (Tables 2 and 5). When training SLayerGen jointly on Alex2D and MP20, we observed higher U.N. and S.U.N. rates on MP20 (Table 5) and nearly identical performance to SLayerGen when only trained on Alex2D (Table 4).

We also found that dynamical Γ phonon stability, ignored in prior generative model evaluations (Zeni et al., 2025; Miller et al., 2024; Chang et al., 2025), significantly decreased stability rates.

Sensitivity analysis and ablations In Table 7, we find that P1-based models deteriorate on symmetry-based metrics as `spglib`'s `symprec` tolerance is tightened, while the SLayerGen model variants maintain performance. We also ablated the effect of modeling aperiodicity along the c-axis (Table 6), finding that modeling diperiodic materials as diperiodic (instead of triperiodic) improves performance.

6 Conclusions

In this paper, we proposed SLayerGen to generate crystals constrained by any space or layer group. We assembled several datasets and proposed evaluation metrics to facilitate progress in generative modeling of diperiodic materials; developed representations for layer groups, Wyckoff positions, and their associated asymmetric units; and built the first layer group invariant generative model, achieving state-of-the-art performance and enabling joint training on bulk and diperiodic materials.

Limitations and future directions We used MLIP predictions as a proxy for DFT, which itself contains physical approximations. We did not explore how jointly training on tri/diperiodic materials might benefit from model scaling or architecture design. Our diperiodic materials stability metrics ignored effects from substrates (Shapera & Schleife, 2018), magnetism, and disorder. Building benchmarks that consider these complexities, possibly with advancements in MLIPs (Ho et al., 2026) and/or physical simulation (Motamarri et al., 2013; 2020; Baek et al., 2025), may help close the gap between *in silico* design and experiment. Other avenues for future research include post-training on symmetry-dependent properties, handling broken symmetries (Finzi et al., 2021), and transfer learning across broad materials classes or properties (Wood et al., 2026; Chang et al., 2022).

AI use statement

In this work, we used generative AI tools for support implementing methods and cleaning datasets. We have not used generative AI tools for generating synthetic data sets, developing theoretical models or conceptual frameworks, formulating mathematical claims, providing critical ingredients for proving mathematical claims, assisting in the writing of proofs, proposing or refining hypotheses, designing or providing feedback on research methodology or experiments, assisting with translation, supporting qualitative and thematic data analysis, or interpreting results. We take responsibility for

the final content of this work, including text, claims or artifacts produced with the aid of generative AI.

REFERENCES

Mohammad A. Akhound, Tara M. Boland, Mikkel O. Sauer, Matthias Batzill, Moses A. Bokinala, Stela Canulescu, Yury Gogotsi, Philip Hofmann, Andras Kis, Jiong Lu, Thomas Michely, Søren Raza, Wencai Ren, Joshua A. Robinson, Zdenek Sofer, Jing H. Teng, Søren Ulstrup, Meng Zhao, Xiaoxu Zhao, Jens J. Mortensen, Thomas Olsen, and Kristian S. Thygesen. Large-scale integration of experimental and computational data for 2d materials, 2026. URL https://arxiv.org/abs/2603.05083.

Omar Allam, Brook Wander, SungYeon Kim, Rudi Plesch, Tyler Sours, Jia-Min Chu, Thomas Ludwig, Jiyoon Kim, Rodrigo Wang, Shivang Agarwal, Alan Rask, Alexandre Fleury, Chuhong Wang, Andrew Wildman, Thomas Mustard, Kevin Ryczko, Paul Abruzzo, AJ Nish, and Aayush R. Singh. Aqcat25: Unlocking spin-aware, high-fidelity machine learning potentials for heterogeneous catalysis, 2025. URL https://arxiv.org/abs/2510.22938.

M.I. Aroyo, H. Burzlaff, G. Chapuis, W. Fischer, H.D. Flack, A.M. Glazer, H. Grimmer, B. Gruber, Th. Hahn, H. Klapper, E. Koch, P. Konstantinov, V. Kopsky, D.B. Litvin, A. Looijenga-Vos, K. Momma, U. Mueller, U. Shmueli, B. Souvignier, J.C.H. Spence, P.M. de Wolff, H. Wondratschek, and H. Zimmerman. *International Tables for Crystallography: Space-group symmetry*, volume A. International Union of Crystallography, Chester, England, 2 edition, 2016. ISBN 978-0-470-97423-0. doi: 10.1107/97809553602060000114. URL https://it.iucr.org/Ac/.

Anton Autere, Henri Jussila, Yunyun Dai, Yadong Wang, Harri Lipsanen, and Zhipei Sun. Nonlinear optics with 2d layered materials. *Advanced Materials*, 30(24):1705963, 2018. doi: https://doi.org/10.1002/adma.201705963. URL https://advanced.onlinelibrary.wiley.com/doi/abs/10.1002/adma.201705963.

Woohyeon Baek, Sambit Das, Shibo Tan, Vikram Gavini, and Wenhao Sun. Quasicrystal stability and nucleation kinetics from density functional theory. *Nature Physics*, 21(6):980–987, June 2025.

Luis Barroso-Luque, Muhammed Shuaibi, Xiang Fu, Brandon M. Wood, Misko Dzamba, Meng Gao, Ammar Rizvi, C. Lawrence Zitnick, and Zachary W. Ulissi. Open materials 2024 (omat24) inorganic materials dataset and models, 2024. URL https://arxiv.org/abs/2410.12771.

Erik Bitzek, Pekka Koskinen, Franz Gähler, Michael Moseler, and Peter Gumbsch. Structural relaxation made simple. *Phys. Rev. Lett.*, 97:170201, Oct 2006. doi: 10.1103/PhysRevLett.97.170201. URL https://link.aps.org/doi/10.1103/PhysRevLett.97.170201.

Lili Cai, Connor J McClellan, Ai Leen Koh, Hong Li, Eilam Yalon, Eric Pop, and Xiaolin Zheng. Rapid flame synthesis of atomically thin MoO3 down to monolayer thickness for effective hole doping of WSe2. *Nano Lett.*, 17(6):3854–3861, June 2017.

Tianle Cai, Shengjie Luo, Keyulu Xu, Di He, Tie yan Liu, and Liwei Wang. Graphnorm: A principled approach to accelerating graph neural network training, 2020.

Yuan Cao, Valla Fatemi, Shiang Fang, Kenji Watanabe, Takashi Taniguchi, Efthimios Kaxiras, and Pablo Jarillo-Herrero. Unconventional superconductivity in magic-angle graphene superlattices. *Nature*, 556(7699):43–50, April 2018.

Zhendong Cao, Xiaoshan Luo, Jian Lv, and Lei Wang. Space group informed transformer for crystalline materials generation, 2024.

Andres Castellanos-Gomez, Xiangfeng Duan, Zhe Fei, Humberto Rodriguez Gutierrez, Yuan Huang, Xinyu Huang, Jorge Quereda, Qi Qian, Eli Sutter, and Peter Sutter. Van der waals heterostructures. *Nature Reviews Methods Primers*, 2(1):58, July 2022.

Gouri Chakraborty, In-Hyeok Park, Raghavender Medishetty, and Jagadese J Vittal. Two-Dimensional Metal-Organic framework materials: Synthesis, structures, properties and applications. *Chem. Rev.*, 121(7):3751–3891, April 2021.

Rees Chang, Yu-Xiong Wang, and Elif Ertekin. Towards overcoming data scarcity in materials science: unifying models and datasets with a mixture of experts framework. *npj Computational Materials*, 8(1):242, November 2022.

Rees Chang, Angela Pak, Alex Guerra, Ni Zhan, Nick Richardson, Elif Ertekin, and Ryan P Adams. Space group equivariant crystal diffusion. In *The Thirty-ninth Annual Conference on Neural Information Processing Systems*, 2025. URL https://openreview.net/forum?id=NWP8KYKC0c.

Gowoon Cheon, Karel-Alexander N Duerloo, Austin D Sendek, Chase Porter, Yuan Chen, and Evan J Reed. Data mining for new two- and One-Dimensional weakly bonded solids and Lattice-Commensurate heterostructures. *Nano Lett.*, 17(3):1915–1923, March 2017.

Stanley S Chou, Na Sai, Ping Lu, Eric N Coker, Sheng Liu, Kateryna Artyushkova, Ting S Luk, Bryan Kaehr, and C Jeffrey Brinker. Understanding catalysis in a multiphasic two-dimensional transition metal dichalcogenide. *Nature Communications*, 6(1):8311, October 2015.

Orion Cohen, Janosh Riebesell, Rhys Goodall, Adeesh Kolluru, Stefano Falletta, Joseph Krause, Jorge Colindres, Gerbrand Ceder, and Abhijeet S Gangan. Torchsim: an efficient atomistic simulation engine in pytorch. *AI for Science*, 1(2):025003, nov 2025. doi: 10.1088/3050-287X/ae1799. URL https://doi.org/10.1088/3050-287X/ae1799.

Laura J Cote, Franklin Kim, and Jiaxing Huang. Langmuir-blodgett assembly of graphite oxide single layers. *J. Am. Chem. Soc.*, 131(3):1043–1049, January 2009.

Daniel W Davies, Keith T Butler, Adam J Jackson, Andrew Morris, Jarvist M Frost, Jonathan M Skelton, and Aron Walsh. Computational Screening of All Stoichiometric Inorganic Materials. *Chem*, 1(4):617–627, 2016. ISSN 2451-9294. doi: https://doi.org/10.1016/j.chempr.2016.09.010. URL https://www.sciencedirect.com/science/article/pii/S2451929416301553.

Giovanni Di Liberto, Ángel Morales-García, and Stefan T Bromley. An unconstrained approach to systematic structural and energetic screening of materials interfaces. *Nature Communications*, 13 (1):6236, October 2022.

Rongzhi Dong, Yuqi Song, Edirisuriya M.D. Siriwardane, and Jianjun Hu. Discovery of 2d materials using transformer network-based generative design. *Advanced Intelligent Systems*, 5:2300141, 2023. doi: 10.1002/aisy.202300141.

Luojun Du, Tawfique Hasan, Andres Castellanos-Gomez, Gui-Bin Liu, Yugui Yao, Chun Ning Lau, and Zhipei Sun. Engineering symmetry breaking in 2D layered materials. *Nature Reviews Physics*, 3(3):193–206, March 2021.

Alexandre Duval, Victor Schmidt, Alex Hernández-García, Santiago Miret, Fragkiskos D. Malliaros, Yoshua Bengio, and David Rolnick. Faenet: Frame averaging equivariant gnn for materials modeling. In *ICML*, pp. 9013–9033, 2023. URL https://proceedings.mlr.press/v202/duval23a.html.

M E Dávila, L Xian, S Cahangirov, A Rubio, and G Le Lay. Germanene: a novel two-dimensional germanium allotrope akin to graphene and silicene. *New Journal of Physics*, 16(9):095002, sep 2014. doi: 10.1088/1367-2630/16/9/095002. URL https://doi.org/10.1088/1367-2630/16/9/095002.

Marc Anton Finzi, Gregory Benton, and Andrew Gordon Wilson. Residual pathway priors for soft equivariance constraints. In A. Beygelzimer, Y. Dauphin, P. Liang, and J. Wortman Vaughan (eds.), *Advances in Neural Information Processing Systems*, 2021. URL https://openreview.net/forum?id=k505ekjMzww.

Scott Fredericks, Kevin Parrish, Dean Sayre, and Qiang Zhu. PyXtal: A Python library for crystal structure generation and symmetry analysis. *Computer Physics Communications*, 261:107810, 2021. ISSN 0010-4655. doi: https://doi.org/10.1016/j.cpc.2020.107810. URL https://www.sciencedirect.com/science/article/pii/S0010465520304057.

Jingheng Fu, Mikael Kuisma, Ask Hjorth Larsen, Kohei Shinohara, Atsushi Togo, and Kristian S Thygesen. Symmetry classification of 2d materials: layer groups versus space groups. *2D Materials*, 11(3):035009, apr 2024a. doi: 10.1088/2053-1583/ad3e0c. URL https://doi.org/10.1088/2053-1583/ad3e0c.

Xiang Fu, Tian Xie, Andrew Scott Rosen, Tommi S. Jaakkola, and Jake Allen Smith. MOFDiff: Coarse-grained diffusion for metal-organic framework design. In *The Twelfth International Conference on Learning Representations*, 2024b. URL https://openreview.net/forum?id=0VBsoluxR2.

Shikun Gao, Qinyuan Huang, Chen Huang, Cheng Li, Kaihao Liu, Baisheng Sa, Yadong Yu, Dezhen Xue, Zhe Liu, and Mengyan Dai. Deep generative model for the inverse design of van der waals heterostructures. *Scientific Reports*, 15(1):23023, July 2025.

Niklas W. A. Gebauer, Michael Gastegger, and Kristof T. Schütt. Symmetry-adapted generation of 3d point sets for the targeted discovery of molecules, 2020. URL https://arxiv.org/abs/1906.00957.

Eli Gerber, Steven B Torrisi, Sara Shabani, Eric Seewald, Jordan Pack, Jennifer E Hoffman, Cory R Dean, Abhay N Pasupathy, and Eun-Ah Kim. High-throughput ab initio design of atomic interfaces using InterMatch. *Nature Communications*, 14(1):7921, December 2023.

Morten Niklas Gjerding, Alireza Taghizadeh, Asbjørn Rasmussen, Sajid Ali, Fabian Bertoldo, Thorsten Deilmann, Nikolaj Rørbæk Knøsgaard, Mads Kruse, Ask Hjorth Larsen, Simone Manti, Thomas Garm Pedersen, Urko Petralanda, Thorbjørn Skovhus, Mark Kamper Svendsen, Jens Jørgen Mortensen, Thomas Olsen, and Kristian Sommer Thygesen. Recent progress of the computational 2d materials database (c2db). *2D Materials*, 8(4):044002, jul 2021. doi: 10.1088/2053-1583/ac1059. URL https://doi.org/10.1088/2053-1583/ac1059.

Rafael Gómez-Bombarelli, Jennifer N Wei, David Duvenaud, José Miguel Hernández-Lobato, Benjamín Sánchez-Lengeling, Dennis Sheberla, Jorge Aguilera-Iparraguirre, Timothy D Hirzel, Ryan P Adams, and Alán Aspuru-Guzik. Automatic chemical design using a Data-Driven continuous representation of molecules. *ACS Cent. Sci.*, 4(2):268–276, February 2018.

Prashun Gorai, Eric S. Toberer, and Vladan Stevanović. Computational identification of promising thermoelectric materials among known quasi-2d binary compounds. *J. Mater. Chem. A*, 4: 11110–11116, 2016. doi: 10.1039/C6TA04121C. URL http://dx.doi.org/10.1039/C6TA04121C.

Stefan Grimme, Stephan Ehrlich, and Lars Goerigk. Effect of the damping function in dispersion corrected density functional theory. *Journal of Computational Chemistry*, 32(7):1456–1465, 2011. doi: https://doi.org/10.1002/jcc.21759. URL https://onlinelibrary.wiley.com/doi/abs/10.1002/jcc.21759.

Ralf W. Grosse-Kunstleve, Buddy Wong, Marat Mustyakimov, and Paul D. Adams. Exact direct-space asymmetric units for the 230 crystallographic space groups. *Acta Crystallogr A*, 67(3):269–275, 2011. ISSN 0108-7673. doi: 10.1107/S0108767311007008. URL //journals.iucr.org/paper?pz5088.

Nate Gruver, Anuroop Sriram, Andrea Madotto, Andrew Gordon Wilson, C. Lawrence Zitnick, and Zachary Ward Ulissi. Fine-tuned language models generate stable inorganic materials as text. In *The Twelfth International Conference on Learning Representations*, 2024. URL https://openreview.net/forum?id=vN9fpfqoP1.

Sten Haastrup, Mikkel Strange, Mohnish Pandey, Thorsten Deilmann, Per S Schmidt, Nicki F Hinsche, Morten N Gjerding, Daniele Torelli, Peter M Larsen, Anders C Riis-Jensen, Jakob Gath, Karsten W Jacobsen, Jens Jørgen Mortensen, Thomas Olsen, and Kristian S Thygesen. The computational 2d materials database: high-throughput modeling and discovery of atomically thin crystals. *2D Materials*, 5(4):042002, sep 2018. doi: 10.1088/2053-1583/aacfc1. URL https://doi.org/10.1088/2053-1583/aacfc1.

Bowen Han and Yongqiang Cheng. Benchmarking universal machine learning interatomic potentials for rapid analysis of inelastic neutron scattering data*. *Machine Learning: Science and Technology*, 6(3):030504, aug 2025. doi: 10.1088/2632-2153/adfa68. URL https://doi.org/10.1088/2632-2153/adfa68.

Cheuk Hin Ho, Cas van der Oord, James P. Darby, Theo Keane, Raz L. Benson, Cristian Rebolledo Espinoza, Rutvij Kulkarni, Elina Spinu, Michail Papanikolaou, Richard Tomsett, Robert M. Forrest, Jonathan J. Bean, Gábor Csányi, and Christoph Ortner. Equivariant many-body message passing interatomic potentials for magnetic materials, 2026. URL https://arxiv.org/abs/2604.08143.

Jordan Hoffmann, Louis Maestrati, Yoshihide Sawada, Jian Tang, Jean Michel Sellier, and Yoshua Bengio. Data-driven approach to encoding and decoding 3-D crystal structures, 2019. URL https://arxiv.org/abs/1909.00949.

Philipp Höllmer, Thomas Egg, Maya Martirossyan, Eric Fuemmeler, Amit Gupta, Zeren Shui, Pawan Prakash, Adrian Roitberg, Mingjie Liu, George Karypis, Mark Transtrum, Richard Hennig, Ellad B. Tadmor, and Stefano Martiniani. Open materials generation with stochastic interpolants. In *AI for Accelerated Materials Design - ICLR 2025*, 2025. URL https://openreview.net/forum?id=ka2jxtCrkK.

Emiel Hoogeboom, Víctor Garcia Satorras, Clément Vignac, and Max Welling. Equivariant diffusion for molecule generation in 3D. In Kamalika Chaudhuri, Stefanie Jegelka, Le Song, Csaba Szepesvari, Gang Niu, and Sivan Sabato (eds.), *Proceedings of the 39th International Conference on Machine Learning*, volume 162 of *Proceedings of Machine Learning Research*, pp. 8867–8887. PMLR, 17–23 Jul 2022. URL https://proceedings.mlr.press/v162/hoogeboom22a.html.

Anubhav Jain, Ping Ong, Geoffroy Hautier, Wei Chen, William Davidson Richards, Stephen Dacek, Shreyas Cholia, Dan Gunter, David Skinner, Gerbrand Ceder, and Kristin A Persson. Commentary: The Materials Project: A materials genome approach to accelerating materials innovation. *APL Mater*, 1:11002, 2013. doi: 10.1063/1.4812323. URL https://doi.org/10.1063/1.4812323.

Junyi Ji, Guoliang Yu, Changsong Xu, and H. J. Xiang. General theory for bilayer stacking ferroelectricity. *Phys. Rev. Lett.*, 130:146801, Apr 2023. doi: 10.1103/PhysRevLett.130.146801. URL https://link.aps.org/doi/10.1103/PhysRevLett.130.146801.

Rui Jiao, Wenbing Huang, Peijia Lin, Jiaqi Han, Pin Chen, Yutong Lu, and Yang Liu. Crystal Structure Prediction by Joint Equivariant Diffusion. In *Thirty-seventh Conference on Neural Information Processing Systems*, 2023.

Rui Jiao, Wenbing Huang, Yu Liu, Deli Zhao, and Yang Liu. Space group constrained crystal generation. In *The Twelfth International Conference on Learning Representations*, 2024. URL https://openreview.net/forum?id=jkvZ7v4OmP.

Bowen Jing, Gabriele Corso, Jeffrey Chang, Regina Barzilay, and Tommi S. Jaakkola. Torsional diffusion for molecular conformer generation. In Alice H. Oh, Alekh Agarwal, Danielle Belgrave, and Kyunghyun Cho (eds.), *Advances in Neural Information Processing Systems*, 2022. URL https://openreview.net/forum?id=w6fj2r62r_H.

Chaitanya K. Joshi, Xiang Fu, Yi-Lun Liao, Vahe Gharakhanyan, Benjamin Kurt Miller, Anuroop Sriram, and Zachary Ward Ulissi. All-atom diffusion transformers. In *AI for Accelerated Materials Design - ICLR 2025*, 2025. URL https://openreview.net/forum?id=mXApCXR2lF.

Tero Karras, Miika Aittala, Timo Aila, and Samuli Laine. Elucidating the design space of diffusion-based generative models. In Alice H. Oh, Alekh Agarwal, Danielle Belgrave, and Kyunghyun Cho (eds.), *Advances in Neural Information Processing Systems*, 2022. URL https://openreview.net/forum?id=k7FuTOWMOc7.

Nikita Kazeev, Ruiming Zhu, Ignat Romanov, Andrey E Ustyuzhanin, Shuya Yamazaki, Wei Nong, and Kedar Hippalgaonkar. Wyckofftransformer: Generation of symmetric crystals. In *AI for Accelerated Materials Design - NeurIPS 2024*, 2024. URL https://openreview.net/forum?id=Jcy1bPOqrY.

Filip Ekström Kelvinius, Oskar B. Andersson, Abhijith S. Parackal, Dong Qian, Rickard Armiento, and Fredrik Lindsten. Wyckoffdiff – a generative diffusion model for crystal symmetry, 2025. URL https://arxiv.org/abs/2502.06485.

Nayoung Kim, Honghui Kim, Sihyun Yu, Minkyu Kim, Seongsu Kim, and Sungsoo Ahn. Atommof: All-atom flow matching for mof-adsorbate structure prediction, 2026. URL https://arxiv.org/abs/2602.07351.

Sungwon Kim, Juhwan Noh, Geun Ho Gu, Alán Aspuru-Guzik, and Yousung Jung. Generative Adversarial Networks for Crystal Structure Prediction. *ACS Central Science*, 6(8):1412–1420, 2020. URL http://arxiv.org/abs/2004.01396.

Diederik P. Kingma and Jimmy Ba. Adam: A method for stochastic optimization. In *ICLR (Poster)*, 2015. URL http://arxiv.org/abs/1412.6980.

Jonas Köhler, Leon Klein, and Frank Noe. Equivariant flows: Exact likelihood generative learning for symmetric densities. In Hal Daumé III and Aarti Singh (eds.), *Proceedings of the 37th International Conference on Machine Learning*, volume 119 of *Proceedings of Machine Learning Research*, pp. 5361–5370. PMLR, 13–18 Jul 2020. URL https://proceedings.mlr.press/v119/kohler20a.html.

Peter Mahler Larsen, Mohnish Pandey, Mikkel Strange, and Karsten Wedel Jacobsen. Definition of a scoring parameter to identify low-dimensional materials components. *Phys. Rev. Mater.*, 3:034003, Mar 2019. doi: 10.1103/PhysRevMaterials.3.034003. URL https://link.aps.org/doi/10.1103/PhysRevMaterials.3.034003.

Daniel S. Levine, Muhammed Shuaibi, Evan Walter Clark Spotte-Smith, Michael G. Taylor, Muhammad R. Hasyim, Kyle Michel, Ilyes Batatia, Gábor Csányi, Misko Dzamba, Peter Eastman, Nathan C. Frey, Xiang Fu, Vahe Gharakhanyan, Aditi S. Krishnapriyan, Joshua A. Rackers, Sanjeev Raja, Ammar Rizvi, Andrew S. Rosen, Zachary Ulissi, Santiago Vargas, C. Lawrence Zitnick, Samuel M. Blau, and Brandon M. Wood. The open molecules 2025 (omol25) dataset, evaluations, and models, 2026. URL https://arxiv.org/abs/2505.08762.

Daniel Levy, Siba Smarak Panigrahi, Sékou-Oumar Kaba, Qiang Zhu, Kin Long Kelvin Lee, Mikhail Galkin, Santiago Miret, and Siamak Ravanbakhsh. SymmCD: Symmetry-preserving crystal generation with diffusion models. In *The Thirteenth International Conference on Learning Representations*, 2025. URL https://openreview.net/forum?id=xnssGv9rpW.

Peijia Lin, Pin Chen, Rui Jiao, Qing Mo, Cen Jianhuan, Wenbing Huang, Yang Liu, Dan Huang, and Yutong Lu. Equivariant diffusion for crystal structure prediction. In *Forty-first International Conference on Machine Learning*, 2024. URL https://openreview.net/forum?id=VRv8KjJNuj.

D.B. Litvin and V. Kopský. *International Tables for Crystallography Volume E: Subperiodic groups*, volume E. International Union of Crystallography, 2 edition, 2010. ISBN 978-0-470-68672-0. doi: 10.1107/97809553602060000109. URL https://it.iucr.org/Eb/.

Antoine Loew, Dewen Sun, Hai-Chen Wang, Silvana Botti, and Miguel A L Marques. Universal machine learning interatomic potentials are ready for phonons. *npj Computational Materials*, 11 (1):178, June 2025.

P. Lyngby and Thygesen K.S. Data-driven discovery of 2d materials by deep generative models. *npj Computational Materials*, 8:232, 2022. doi: 10.1038/s41524-022-00923-3.

Benjamin Kurt Miller, Ricky T.Q. Chen, Anuroop Sriram, and Brandon M. Wood. FlowMM: Generating Materials with Riemannian Flow Matching. *Proceedings of Machine Learning Research*, 235: 35664–35686, 2024. ISSN 26403498. URL https://arxiv.org/abs/2406.04713v1.

Mehran Mirramezani, Anne S. Meeussen, Katia Bertoldi, Peter Orbanz, and Ryan P Adams. Designing mechanical meta-materials by learning equivariant flows. In *The Thirteenth International Conference on Learning Representations*, 2025. URL https://openreview.net/forum?id=VMurwgAFWP.

Mistal, Alex Hernández-García, Alexandra Volokhova, Alexandre AGM Duval, Yoshua Bengio, Divya Sharma, Pierre Luc Carrier, Michał Koziarski, and Victor Schmidt. Crystal-GFN: sampling materials with desirable properties and constraints. In *AI for Accelerated Materials Design - NeurIPS 2023 Workshop*, 2023. URL https://openreview.net/forum?id=l167FjdPOv.

P. Motamarri, M.R. Nowak, K. Leiter, J. Knap, and V. Gavini. Higher-order adaptive finite-element methods for kohn–sham density functional theory. *Journal of Computational Physics*, 253:308–343, 2013. ISSN 0021-9991. doi: https://doi.org/10.1016/j.jcp.2013.06.042. URL https://www.sciencedirect.com/science/article/pii/S0021999113004774.

Phani Motamarri, Sambit Das, Shiva Rudraraju, Krishnendu Ghosh, Denis Davydov, and Vikram Gavini. Dft-fe – a massively parallel adaptive finite-element code for large-scale density functional theory calculations. *Computer Physics Communications*, 246:106853, 2020. ISSN 0010-4655. doi: https://doi.org/10.1016/j.cpc.2019.07.016. URL https://www.sciencedirect.com/science/article/pii/S0010465519302309.

Nicolas Mounet, Marco Gibertini, Philippe Schwaller, Davide Campi, Andrius Merkys, Antimo Marrazzo, Thibault Sohier, Ivano Eligio Castelli, Andrea Cepellotti, Giovanni Pizzi, and Nicola Marzari. Two-dimensional materials from high-throughput computational exfoliation of experimentally known compounds. *Nature Nanotechnology*, 13(3):246–252, March 2018.

K. S. Novoselov, A. K. Geim, S. V. Morozov, D. Jiang, Y. Zhang, S. V. Dubonos, I. V. Grigorieva, and A. A. Firsov. Electric field effect in atomically thin carbon films. *Science*, 306(5696):666–669, 2004. doi: 10.1126/science.1102896. URL https://www.science.org/doi/abs/10.1126/science.1102896.

K. S. Novoselov, A. Mishchenko, A. Carvalho, and A. H. Castro Neto. 2d materials and van der waals heterostructures. *Science*, 353(6298):aac9439, 2016. doi: 10.1126/science.aac9439. URL https://www.science.org/doi/abs/10.1126/science.aac9439.

Shyue Ping Ong, William Davidson Richards, Anubhav Jain, Geoffroy Hautier, Michael Kocher, Shreyas Cholia, Dan Gunter, Vincent L. Chevrier, Kristin A. Persson, and Gerbrand Ceder. Python Materials Genomics (pymatgen): A robust, open-source python library for materials analysis. *Computational Materials Science*, 68:314–319, 2013. ISSN 09270256. doi: 10.1016/j.commatsci.2012.10.028.

Sahar Pakdel, Asbjørn Rasmussen, Alireza Taghizadeh, Mads Kruse, Thomas Olsen, and Kristian S Thygesen. High-throughput computational stacking reveals emergent properties in natural van der waals bilayers. *Nature Communications*, 15(1):932, January 2024.

Hyunsoo Park, Anthony Onwuli, and Aron Walsh. Exploration of crystal chemical space using text-guided generative artificial intelligence. *Nature Communications*, 16(1):4379, 2025. doi: 10.1038/s41467-025-59636-y. URL https://doi.org/10.1038/s41467-025-59636-y.

K. Parlinski, Z. Q. Li, and Y. Kawazoe. First-principles determination of the soft mode in cubic zro_2. *Phys. Rev. Lett.*, 78:4063–4066, May 1997. doi: 10.1103/PhysRevLett.78.4063. URL https://link.aps.org/doi/10.1103/PhysRevLett.78.4063.

Omri Puny, Matan Atzmon, Edward J. Smith, Ishan Misra, Aditya Grover, Heli Ben-Hamu, and Yaron Lipman. Frame averaging for invariant and equivariant network design. In *International Conference on Learning Representations*, 2022. URL https://openreview.net/forum?id=zIUyj55nXR.

Omri Puny, Yaron Lipman, and Benjamin Kurt Miller. Space group conditional flow matching, 2025. URL https://arxiv.org/abs/2509.23822.

Zekun Ren, Juhwan Noh, Siyu Tian, Felipe Oviedo, Guangzong Xing, Qiaohao Liang, Armin Aberle, Yi Liu, Qianxiao Li, Senthilnath Jayavelu, Kedar Hippalgaonkar, Yousung Jung, and Tonio Buonassisi. Inverse design of crystals using generalized invertible crystallographic representation. *Matter*, 5(1), 2022. URL https://arxiv.org/abs/2005.07609.

Danilo Jimenez Rezende, Sébastien Racanière, Irina Higgins, and Peter Toth. Equivariant hamiltonian flows, 2019. URL https://arxiv.org/abs/1909.13739.

Benjamin Rhodes, Sander Vandenhaute, Vaidotas Šimkus, James Gin, Jonathan Godwin, Tim Duignan, and Mark Neumann. Orb-v3: atomistic simulation at scale, 2025. URL https://arxiv.org/abs/2504.06231.

Laura Ruple, Luca Torresi, Henrik Schopmans, and Pascal Friederich. Symmetry-aware bayesian flow networks for crystal generation, 2025. URL https://arxiv.org/abs/2502.03146.

Yu Saito, Tsutomu Nojima, and Yoshihiro Iwasa. Highly crystalline 2D superconductors. *Nature Reviews Materials*, 2(1):16094, December 2016.

Mikkel Ohm Sauer, Peder Meisner Lyngby, and Kristian Sommer Thygesen. Dispersion-corrected machine learning potentials for 2d van der waals materials. *Phys. Rev. Mater.*, 9:074007, Jul 2025. doi: 10.1103/cl8c-8f1f. URL https://link.aps.org/doi/10.1103/cl8c-8f1f.

John R Schaibley, Hongyi Yu, Genevieve Clark, Pasqual Rivera, Jason S Ross, Kyle L Seyler, Wang Yao, and Xiaodong Xu. Valleytronics in 2D materials. *Nature Reviews Materials*, 1(11):16055, August 2016.

Jonathan Schmidt, Tiago F.T. Cerqueira, Aldo H. Romero, Antoine Loew, Fabian Jäger, Hai-Chen Wang, Silvana Botti, and Miguel A.L. Marques. Improving machine-learning models in materials science through large datasets. *Materials Today Physics*, 48:101560, 2024. ISSN 2542-5293. doi: https://doi.org/10.1016/j.mtphys.2024.101560. URL https://www.sciencedirect.com/science/article/pii/S2542529324002360.

Ethan P. Shapera and André Schleife. Database-driven materials selection for semiconductor heterojunction design. *Advanced Theory and Simulations*, 1(10):1800075, 2018. doi: https://doi.org/10.1002/adts.201800075. URL https://advanced.onlinelibrary.wiley.com/doi/abs/10.1002/adts.201800075.

Chence Shi, Shitong Luo, Minkai Xu, and Jian Tang. Learning gradient fields for molecular conformation generation. In Marina Meila and Tong Zhang (eds.), *Proceedings of the 38th International Conference on Machine Learning*, volume 139 of *Proceedings of Machine Learning Research*, pp. 9558–9568. PMLR, 18–24 Jul 2021. URL https://proceedings.mlr.press/v139/shi21b.html.

Vaidotas Simkus, Anders Christensen, Steven Bennett, Ian Johnson, Mark Neumann, James Gin, Jonathan Godwin, and Benjamin Rhodes. Mofasa: A step change in metal-organic framework generation, 2025. URL https://arxiv.org/abs/2512.01756.

Junki Sone, Tsuyoshi Yamagami, Yuki Aoki, Kan Nakatsuji, and Hiroyuki Hirayama. Epitaxial growth of silicene on ultra-thin ag(111) films. *New Journal of Physics*, 16(9):095004, sep 2014. doi: 10.1088/1367-2630/16/9/095004. URL https://doi.org/10.1088/1367-2630/16/9/095004.

Yang Song and Stefano Ermon. Generative Modeling by Estimating Gradients of the Data Distribution. In *Advances in Neural Information Processing Systems*, 2019.

Yang Song, Jascha Sohl-Dickstein, Diederik P Kingma, Abhishek Kumar, Stefano Ermon, and Ben Poole. Score-based generative modeling through stochastic differential equations. In *International Conference on Learning Representations*, 2021. URL https://openreview.net/forum?id=PxTIG12RRHS.

Anuroop Sriram, Benjamin Kurt Miller, Ricky T. Q. Chen, and Brandon M Wood. FlowLLM: Flow matching for material generation with large language models as base distributions. In *The Thirty-eighth Annual Conference on Neural Information Processing Systems*, 2024. URL https://openreview.net/forum?id=0bFXbEMz8e.

Anuroop Sriram, Logan M. Brabson, Xiaohan Yu, Sihoon Choi, Kareem Abdelmaqsoud, Elias Moubarak, Pim de Haan, Sindy Löwe, Johann Brehmer, John R. Kitchin, Max Welling, C. Lawrence Zitnick, Zachary Ulissi, Andrew J. Medford, and David S. Sholl. The open dac 2025 dataset for sorbent discovery in direct air capture, 2025. URL https://arxiv.org/abs/2508.03162.

C. Bane Sullivan and Alexander A. Kaszynski. Pyvista: 3d plotting and mesh analysis through a streamlined interface for the visualization toolkit (vtk). *Journal of Open Source Software*, 4(37): 1450, 2019. doi: 10.21105/joss.01450. URL https://doi.org/10.21105/joss.01450.

Wenhao Sun, Stephen T. Dacek, Shyue Ping Ong, Geoffroy Hautier, Anubhav Jain, William D. Richards, Anthony C. Gamst, Kristin A. Persson, and Gerbrand Ceder. The thermodynamic scale of inorganic crystalline metastability. *Science Advances*, 2(11):e1600225, 2016. doi: 10.1126/sciadv.1600225. URL https://www.science.org/doi/abs/10.1126/sciadv.1600225.

Atsushi Togo, Kohei Shinohara, and Isao Tanaka. Spglib: a software library for crystal symmetry search. *Science and Technology of Advanced Materials: Methods*, 4:1, 2024. doi: 10.1080/27660400.2024.2384822. URL https://www.tandfonline.com/doi/abs/10.1080/27660400.2024.2384822.

Richard Tran, Zihan Xu, Balachandran Radhakrishnan, Donald Winston, Wenhao Sun, Kristin A Persson, and Shyue Ping Ong. Surface energies of elemental crystals. *Scientific Data*, 3(1):160080, September 2016.

Di Wang, Feng Tang, Jialin Ji, Wenqing Zhang, Ashvin Vishwanath, Hoi Chun Po, and Xiangang Wan. Two-dimensional topological materials discovery by symmetry-indicator method. *Phys. Rev. B*, 100:195108, Nov 2019. doi: 10.1103/PhysRevB.100.195108. URL https://link.aps.org/doi/10.1103/PhysRevB.100.195108.

Hai-Chen Wang, Jonathan Schmidt, Miguel A L Marques, Ludger Wirtz, and Aldo H Romero. Symmetry-based computational search for novel binary and ternary 2d materials. *2D Materials*, 10 (3):035007, apr 2023. doi: 10.1088/2053-1583/accc43. URL https://doi.org/10.1088/2053-1583/accc43.

Benjamin J. Wieder and C. L. Kane. Spin-orbit semimetals in the layer groups. *Phys. Rev. B*, 94: 155108, Oct 2016. doi: 10.1103/PhysRevB.94.155108. URL https://link.aps.org/doi/10.1103/PhysRevB.94.155108.

Brandon M Wood, Misko Dzamba, Xiang Fu, Meng Gao, Muhammed Shuaibi, Luis Barroso-Luque, Kareem Abdelmaqsoud, Vahe Gharakhanyan, John R. Kitchin, Daniel S. Levine, Kyle Michel, Anuroop Sriram, Taco Cohen, Abhishek Das, Sushree Jagriti Sahoo, Ammar Rizvi, Zachary Ward Ulissi, and C. Lawrence Zitnick. UMA: A family of universal models for atoms. In *The Thirty-ninth Annual Conference on Neural Information Processing Systems*, 2026. URL https://openreview.net/forum?id=SvopaNxYWt.

Hanlin Wu, Yuxuan Song, Jingjing Gong, Ziyao Cao, Yawen Ouyang, Jianbing Zhang, Hao Zhou, Wei-Ying Ma, and Jingjing Liu. A periodic bayesian flow for material generation. In *The Thirteenth International Conference on Learning Representations*, 2025. URL https://openreview.net/forum?id=Lz0XW99tE0.

Kevin E Wu, Kevin K Yang, Rianne van den Berg, Sarah Alamdari, James Y Zou, Alex X Lu, and Ava P Amini. Protein structure generation via folding diffusion. *Nature Communications*, 15(1): 1059, February 2024.

Tian Xie, Xiang Fu, Octavian-Eugen Ganea, Regina Barzilay, and Tommi Jaakkola. Crystal Diffusion Variational Autoencoder for Periodic Material Generation. In *International Conference on Learning Representations*, 2022.

Minkai Xu, Lantao Yu, Yang Song, Chence Shi, Stefano Ermon, and Jian Tang. Geodiff: A geometric diffusion model for molecular conformation generation. In *International Conference on Learning Representations*, 2022. URL https://openreview.net/forum?id=PzcvxEMzvQC.

Shihang Xu, Shibing Chu, Rami Mrad, Zhejun Zhang, Zhelin Li, Runxian Jiao, and Yuanping Chen. Discovery of 2D materials via Symmetry-Constrained diffusion model. *J. Phys. Chem. C*, 129(14): 6794–6802, April 2025.

Keqiang Yan, Xiner Li, Hongyi Ling, Kenna Ashen, Carl Edwards, Raymundo Arroyave, Marinka Zitnik, Heng Ji, Xiaofeng Qian, Xiaoning Qian, and Shuiwang Ji. Invariant tokenization of crystalline materials for language model enabled generation. In *The Thirty-eighth Annual Conference on*

Neural Information Processing Systems, 2024. URL https://openreview.net/forum?id=18FGRNd0wZ.

Sherry Yang, Simon Batzner, Ruiqi Gao, Muratahan Aykol, Alexander L Gaunt, Brendan McMorrow, Danilo J Rezende, Dale Schuurmans, Igor Mordatch, and Ekin D Cubuk. Generative hierarchical materials search. *arXiv preprint arXiv:2409.06762*, 2024a.

Sherry Yang, KwangHwan Cho, Amil Merchant, Pieter Abbeel, Dale Schuurmans, Igor Mordatch, and Ekin Dogus Cubuk. Scalable diffusion for materials generation. In *The Twelfth International Conference on Learning Representations*, 2024b. URL https://openreview.net/forum?id=wm4WlHoXpC.

Dmitry Yarotsky. Universal Approximations of Invariant Maps by Neural Networks. *Constructive Approximation*, 55(1):407–474, 2022. ISSN 1432-0940. doi: 10.1007/s00365-021-09546-1. URL https://doi.org/10.1007/s00365-021-09546-1.

Claudio Zeni, Robert Pinsler, Daniel Zügner, Andrew Fowler, Matthew Horton, Xiang Fu, Aliaksandra Shysheya, Jonathan Crabbé, Lixin Sun, Jake Smith, Bichlien Nguyen, Hannes Schulz, Sarah Lewis, Chin-Wei Huang, Ziheng Lu, Yichi Zhou, Han Yang, Hongxia Hao, Jielan Li, Ryota Tomioka, and Tian Xie. A generative model for inorganic materials design. *Nature*, 2025. URL https://arxiv.org/abs/2312.03687v2.

Jun Zhou, Lei Shen, Miguel Dias Costa, Kristin A Persson, Shyue Ping Ong, Patrick Huck, Yunhao Lu, Xiaoyang Ma, Yiming Chen, Hanmei Tang, and Yuan Ping Feng. 2DMatPedia, an open computational database of two-dimensional materials from top-down and bottom-up approaches. *Scientific Data*, 6(1):86, June 2019.

Ruiming Zhu, Wei Nong, Shuya Yamazaki, and Kedar Hippalgaonkar. WyCryst: Wyckoff inorganic crystal generator framework. *Matter*, 7(10):3469–3488, 2024. ISSN 2590-2393. doi: 10.1016/j.matt.2024.05.042. URL https://doi.org/10.1016/j.matt.2024.05.042.

7 APPENDIX

7.1 DATA PROCESSING

We filtered materials from each dataset that are unlikely to be synthesizable. Based on an analysis of experimentally known monolayers (Haastrup et al., 2018), structures from C2DB and Alex2D were removed if their reported DFT energies above the hull were greater than 200 meV/atom. Since 2DMatPedia used a different DFT functional (vdW-optB88), we filtered that dataset with a cutoff of 150 meV/atom, also determined from known monolayers (Zhou et al., 2019). We filtered BiDB bilayers based on their reported thermodynamic binding stabilities with respect to isolated layers ($E_b = E_{\text{bilayer}} - 2E_{\text{monolayer}} < 0$) and dynamical stabilities with respect to interlayer sliding.

All datasets were further filtered by removing structures predicted to be dynamically unstable with respect to lattice commensurate vibrations, i.e., Γ-point phonons. Dynamical stability was determined by the finite displacement method (Parlinski et al., 1997) under the harmonic approximation with a foundation machine learning interatomic potential (MLIP) accelerated by `torchsim` (Cohen et al., 2025). Specifically, we used `orb_v3_conservative_inf_mpa` (Rhodes et al., 2025) for 2DMatPedia, C2DB, and Alex2D, and `orb_v3_conservative_inf_omat` with BJ-damped D3 corrections (Grimme et al., 2011) for BiDB to account for interlayer van der Waals forces. We highlight that Orb v3 was found to yield state-of-the-art phonon frequency predictions (MAEs <5 meV compared to PBE DFT calculations) on a benchmark of 5000 stable crystals covering 86 elements (Han & Cheng, 2025), and its predecessor Orb v2 was found to excel at structure optimization in heterobilayers (Sauer et al., 2025). We verified these claims by calculating F1 scores for Orb v3 when predicting thermodynamic stability on these datasets, finding significantly higher performance than a dummy classifier that predicts everything is stable (Table 9). Following Loew et al. (2025), we considered a structure dynamically stable with respect to Γ-point phonons if all frequencies were real except for the three acoustic modes, which were allowed to have small imaginary frequencies of -50 K to account for numerical errors.

We note that our filtering tolerances are purposely looser than typical for bulk crystals (Sun et al., 2016); the convex hulls here merely serve as a rough guide for stability of diperiodic materials as surface and interfacial interactions were neglected. Correspondingly, many free-standing diperiodic structures with large energies above the hull and/or unstable phonons have been experimentally realized using substrate materials (Zhou et al., 2019; Sone et al., 2014; Dávila et al., 2014; Cai et al., 2017), metal ion intercalation (Chou et al., 2015), or self-assembly in solution (Cote et al., 2009).

7.2 ABLATING THE EFFECT OF MODELING PERIODICITY ALONG THE *c* AXIS

Table 6: Results for the P1-conditioned SLayerGen variants on the 2DMatPedia and Alex2D datasets.

Dataset	Model	Validity (%) ↑		U.N. rate (%) ↑		Distribution distance ↓				Stable (%) ↑		S.U.N. (%) ↑	
		Structure	Composition	Structure	Template	$W_{\text{Thickness}}$	W_ρ	$W_{N_{\text{el}}}$	JSD_G	E_{hull}	$\text{E}_{\text{hull}}\Gamma$	Structure	Template
2DMatPedia	SLayerGen3D-P1	96.9	52.5	95.7	14.0	1.708	0.078	0.211	0.720	37.8	31.5	27.0	7.3
	SLayerGen-P1	98.6	59.9	94.6	19.1	1.637	0.088	0.154	0.642	41.3	34.1	28.5	8.0
	SLayerGen3D	93.4 ± 1.0	71.7 ± 0.3	91.8 ± 0.8	27.3 ± 1.8	2.005 ± 0.210	0.063 ± 0.005	0.185 ± 0.058	0.208 ± 0.011	36.5 ± 1.0	29.4 ± 1.5	21.3 ± 1.3	4.7 ± 0.9
	SLayerGen	98.4 ± 0.4	70.8 ± 0.4	90.9 ± 1.6	30.3 ± 0.9	1.167 ± 0.007	0.052 ± 0.007	0.195 ± 0.013	0.200 ± 0.008	42.8 ± 1.8	33.2 ± 0.4	24.5 ± 0.9	5.8 ± 0.4
Alex2D	SLayerGen3D-P1	99.4	67.1	74.0	4.9	0.135	0.014	0.144	0.666	78.9	70.0	46.8	3.8
	SLayerGen-P1	98.9	73.0	69.6	8.0	0.209	0.028	0.112	0.500	79.6	72.1	44.9	5.4
	SLayerGen3D	99.5	76.0	68.4	7.5	0.262	0.007	0.080	0.124	76.9	65.1	35.9	2.0
	SLayerGen	99.9	76.9	70.7	7.5	0.143	0.010	0.148	0.149	75.4	63.9	34.2	2.1

From Table 6, we found SLayerGen-P1 exhibited higher (S)UN template rates, a better JSD for layer groups, and slightly higher stability rates than SLayerGen3D-P1, demonstrating that "turning off" periodicity has a positive effect on performance. Interestingly, we also found that SLayerGen-P1 attained a higher SUN template rate than the SLayerGen model, but at the cost of a substantially worse JSD over layer groups (as expected) and composition validity rate (likely due to the need to model more atoms). A possible reason for this result is that the unconstrained P1 model can learn from all three spatial dimensions of every ground truth atom position, while SLayerGen does not learn to move Wyckoff-constrained spatial dimensions (effectively seeing less data) but more faithfully reproduces the data's symmetry distributions and enables explicit control over which layer groups are generated.

To leverage the strengths of both SLayerGen-P1 and SLayerGen, we highlight that SLayerGen could be jointly trained on both P1 and high symmetry layer group representations of materials as a form

of data augmentation. We leave this for future work. We also note that much of the gap in SUN template rates between SLayerGen-P1 and SLayerGen are closed by the "SLayerGen ($T_{G,W} = 2.0$)" model variant (SLayerGen-P1 does not permit tempering of the layer group or Wyckoff position generation).

7.3 SYMMETRY-FINDING SENSITIVITY ANALYSIS

Table 7: Sensitivity analysis of the `symprec` tolerance used for symmetry finding on the 2DMatPedia dataset, computed with two symmetry-detection tolerances. We observed the layer group JSD results to be insensitive to decreasing the tolerance to 0.01 Angstroms. However, the P1-based models (DiffCSP and MatterGen) show noticeably lower performance on (S.)U.N. template rates, while the SLayerGen model variants notably maintain performance. Note that uniqueness/novelty was calculated before relaxation for the U.N. rate and after relaxation for the S.U.N. rate.

	symprec=0.01			symprec=0.1		
Model	U.N. template rate	Layer group JSD	S.U.N. template rate	U.N. template rate	Layer group JSD	S.U.N. template rate
DiffCSP	0.7	0.749	0.8	9.4	0.762	2.4
DiffCSP++	8.3	0.180	2.7	6.3	0.180	3.9
MatterGen	1.3	0.741	2.2	9.8	0.701	4.2
SLayerGen3D	26.7	0.216	3.8	27.3 ± 1.8	0.208 ± 0.011	4.7 ± 0.9
SLayerGen	30.0	0.197	4.5	30.3 ± 0.9	0.200 ± 0.008	5.8 ± 0.4
SLayerGen ($T_{G,W} = 2.0$)	47.6	0.282	4.7	48.0	0.319	7.0

7.4 PERFORMANCE ON LAYER GROUPS THAT DON'T INJECTIVELY MAP TO A SPACE GROUP

Table 8: JSD between generated and reference distributions over non-injective layer groups (`symprec`=0.01), across four datasets.

Dataset	Model	JSD Non-Injective Layer Groups ↓
2DMatPedia	SLayerGen	0.257
	SLayerGen3D	0.293
	MatterGen	0.833
	DiffCSP	0.833
	DiffCSP++	0.311
C2DB	SLayerGen	0.130
	SLayerGen3D	0.217
	SGEquiDiff	0.510
	MatterGen	0.593
	DiffCSP++	0.252
	DiffCSP	0.628
BiDB	SLayerGen	0.184
	SLayerGen3D	0.321
	DiffCSP	0.833
	DiffCSP++	0.374
	MatterGen	0.535
Alex2D	SLayerGen	0.095
	SLayerGen3D	0.156
	MatterGen	0.645
	DiffCSP	0.661
	DiffCSP++	0.202

7.5 ORB-V3

Table 9: F1 scores for Orb-v3 using Materials Project `v2023.02.07` convex hulls on 2,000 random data samples and for a dummy classifier predicting everything as stable on full unfiltered datasets. Stability was defined as having an energy above the hull less than 200 meV/atom. We excluded evaluation on the BiDB dataset because it only contains bilayers with stable binding energies, rendering F1 scores meaningless.

	2DMatPedia		C2DB		Alex2D	
	Orb-v3	Dummy	Orb-v3	Dummy	Orb-v3	Dummy
F1 Score	0.914	0.723	0.903	0.726	0.825	0.480

7.6 EXAMPLES OF SUN TEMPLATES

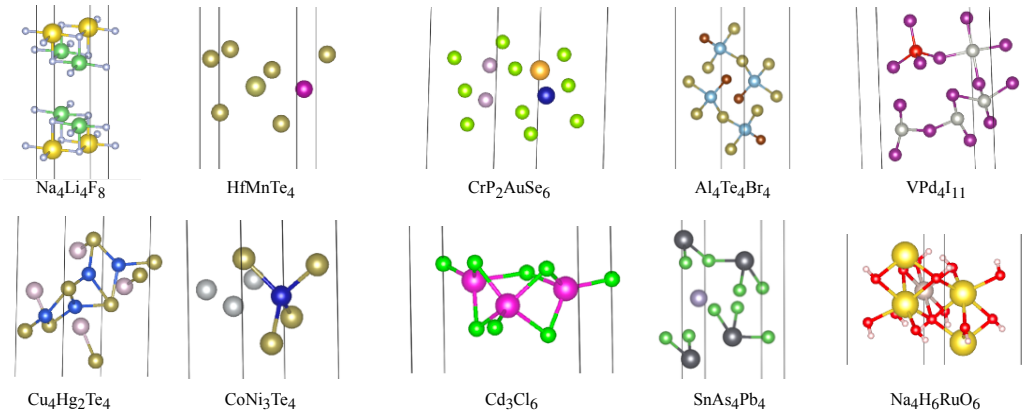


Figure 3: Example conventional unit cells of diperiodic materials generated by SLayerGen that passed our stability filters and had novel templates relative to the Alex2D training dataset. Some atoms have been translated outside the unit cell for visualization purposes.

7.7 SPACE GROUP LATTICE CONSTRAINTS

For conventional unit cells of with lattice lengths $(a = ||L_1||_2, b = ||L_2||_2, c = ||L_3||_2)$ and angles $(\alpha = \angle L_2L_3, \beta = \angle L_1L_3, \gamma = \angle L_1L_2)$, triclinic layer groups 1-2 impose no constraints, monoclinic oblique layer groups 3-7 require $\alpha = \beta = 90°$, monoclinic rectangular layer groups 8-18 require $\beta = \gamma = 90°$, orthorhombic layer groups 19-48 require $\alpha = \beta = \gamma = 90°$, tetragonal layer groups 49-64 require $a = b$ and $\alpha = \beta = \gamma = 90°$, and hexagonal layer groups 65-80 require $a = b$ and $\alpha = \beta = 90°$ and $\gamma = 120°$ (Fu et al., 2024a).

Space groups 1 to 2 impose no constraints on the lattice; 3 to 15 require $\alpha = \gamma = 90°$; 16 to 74 require $\alpha = \beta = \gamma = 90°$; 75 to 142 require $\alpha = \beta = \gamma = 90°$ and $a = b$; 143 to 194 require $a = b$, $\alpha = \beta = 90°$, and $\gamma = 120°$; and 195 to 230 require $a = b = c$ and $\alpha = \beta = \gamma = 90°$. The entantiomorphic space groups require $|L| > 0$ and consist of groups 76, 79, 91, 92, 95, 96, 144, 145, 151-154, 169-172, 178-181, 212, and 213.

7.8 REMOVING REDUNDANCY FROM LAYER GROUP WYCKOFF POSITIONS

We enumerated symmetrically unique regions of every Wyckoff position across the 80 layer groups. Since these can be found immediately for general Wyckoff positions as the interiors of the asymmetric units, we focus on the special Wyckoff positions which lie on asymmetric unit boundaries. For these, we first projected random points in $[0, 1]^3$ onto special Wyckoff positions using projection matrices from `PyXtal` (Fredericks et al., 2021) and then intersected the resulting points/lines/planes with

the inexact ASUs from the International Tables of Crystallography (Litvin & Kopský, 2010) using `sympy`. To make these intersections *exact*, we visually inspected the corresponding shapes in their asymmetric units using `PyVista` (Sullivan & Kaszynski, 2019) and manually edited the shape vertices. For each Wyckoff position, we validated the completeness and uniqueness of the resulting shapes under layer group symmetry by projecting 1000 uniform random points in $[0, 1]^3$ onto the Wyckoff position with `PyXtal` and asserting that each point's orbit lands within machine precision of our shape(s) exactly once.

During processing of the Wyckoff positions, we discovered two errors in the International Tables of Crystallography (Litvin & Kopský, 2010). First, we observed that the inexact asymmetric unit for layer group 7, listed as $0 \leq x \leq 1/2;\ 0 \leq y \leq 1/2; 0 \leq z$, does not tile $\mathbb{R}^3$ upon application of the group actions. We corrected this asymmetric unit to $0 \leq x \leq 1/2;\ 0 \leq y \leq 1/2$, as shown in Fig. 4. Second, we found that the inexact asymmetric unit for layer group 46 was listed as $0 \leq x \leq 1/4;\ 0 \leq y \leq 1/2$, which erroneously contained points from special Wyckoff position 4e in the asymmetric unit interior. Specifically, Wyckoff position 4e is defined at points $(x, \frac{1}{4}, z)\ \forall x, z \in \mathbb{R}$, which clearly resides in the asymmetric interior, for example, at $x = 1/8$ and any z. By manual inspection, we corrected this inexact asymmetric unit to $1/4 \leq x \leq 3/4;\ 0 \leq y \leq 1/4$.

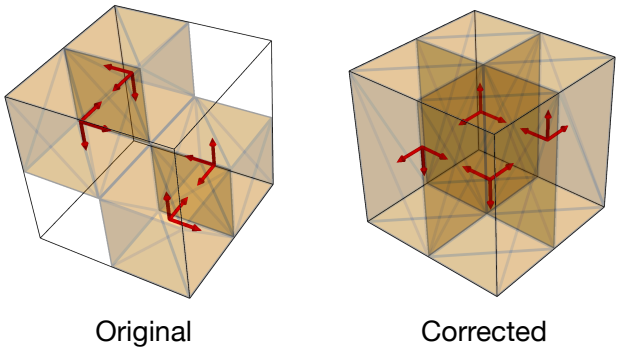


Figure 4: Left: The asymmetric unit (orange) listed by the International Tables of Crystallography for layer group 7, orbited by the layer group actions modulo lattice translations. We included an asymmetric object (red) at the center of each orbited asymmetric unit to visualize orientation. The conventional unit cell, outlined in black, is truncated to $z \in [-\frac{1}{2}, \frac{1}{2}]$ for visualization. The listed asymmetric unit does not tile $\mathbb{R}^3$. Right: Our asymmetric unit definition tiles $\mathbb{R}^3$.

7.8.1 Representing layer groups and their Wyckoff positions

To encourage learning correlations between different space and layer groups, we modified the space group and Wyckoff position embeddings from SGEquiDiff (Chang et al., 2025) and extended them for layer groups. Specifically, space and layer groups were represented as the concatenation of 6-dimensional one-hot lattice centerings, 6-dimensional one-hot crystal families, 32-dimensional one-hot crystallographic point groups, a 1-dimensional indicator of whether the group supports chiral structures, a 1-dimensional indicator of whether the group is centrosymmetric, a 3-dimensional indicator of whether each lattice axis is periodic, and 16-dimensional arbitrary one-hot features to avoid collisions between groups resulting from having ignored screw and glide symmetries. This yielded $6 + 6 + 32 + 1 + 1 + 3 + 16 = 65$ total features per group. Each Wyckoff position was represented as the concatenation of the 65-dimensional crystallographic group embedding, 78-dimensional one-hot site symmetry group symbols, 4-dimensional indicators of how many degrees of freedom in the atomic coordinates are allowed by the Wyckoff position (i.e., 0-3), 17-dimensional one-hot Wyckoff multiplicities, and 48-dimensional mean-pooled Fourier embeddings of the centroids and vertices of the Wyckoff shapes, yielding $65 + 78 + 4 + 17 + 48 = 212$ features.

7.9 CRYSTALLOGRAPHIC GROUP WRAPPED NORMAL

Proof sketch of score equivariance for layer groups For isotropic Σ_t and orthogonal R, Chang et al. (2025) proved that the score of the GWN is equivariant, i.e.,

$$\nabla_{x_t} \log p(Rx_t + v|x_0; \Sigma_t) = R\nabla_{x_t} \log p(x_t|x_0; \Sigma_t). \tag{6}$$

This result also holds for the layer groups with our choice of anisotropic covariance $\Sigma_t = \sigma_{xy}^2 I_2 \bigoplus \sigma_z^2 I_1$. Specifically, since R is block diagonal, i.e., $R = R^{xy} \bigoplus R^z$ for $R^{xy} \in O(2)$ and $R^z \in O(1)$, then the proof of Chang et al. (2025) directly applies to each subspace independently.

Non-orthogonality in fractional coordinates for hexagonal groups While all crystallographic groups strictly contain isometries in real space, when working in fractional coordinates, hexagonal groups contain group elements $g = \{R_g, v_g\}$ where $R_g \notin O(3)$. These groups have conventional lattice parameter constraints following $a = b$, $\alpha = \beta = 90°$, and $\gamma = 120°$, yielding lattice matrices of the form

$$L = \begin{pmatrix} a & -a/2 & 0 \\ 0 & a\sqrt{3}/2 & 0 \\ 0 & 0 & c \end{pmatrix}$$

where each column is a lattice vector. Naively, using L, we could compute our Group Wrapped Normal in the Cartesian basis where group representations are orthogonal. However, we wish for scores of the Group Wrapped Normal to be invariant to the lattice size so that we can choose a single noise scheduler for all crystals. Thus, for hexagonal groups, we choose the following canonical basis:

$$B = \begin{pmatrix} 1 & -1/2 & 0 \\ 0 & \sqrt{3}/2 & 0 \\ 0 & 0 & 1 \end{pmatrix}.$$

In this basis, given $g = \{R, v\}$ where R and v act on fractional positions $x \in \mathbb{R}^3$, group actions become

$$\begin{aligned} B(Rx + v) &= (BRB^{-1})(Bx) + Bv \\ &\equiv \tilde{R}\tilde{x} + \tilde{v} \end{aligned}$$

where $\tilde{R} = BRB^{-1} \in O(3)$, $\tilde{x} = Bx$, and $\tilde{v} = Bv$. We compute scores $\nabla_{\tilde{x}_t} \log p(\tilde{x}_t|\tilde{x}_0)$ the same way as SGEquiDiff (Chang et al., 2025) but plug in our transformed variables:

$$\begin{aligned} \nabla_{\tilde{x}_t} \log p(\tilde{x}_t|\tilde{x}_0) &= \frac{\sum_{\{R_j, v_j\} \in G} \exp\left(\frac{-[\tilde{x}_t - (\tilde{R}_j\tilde{x}_0 + \tilde{v}_j)]^T \Sigma_t^{-1} [\tilde{x}_t - (\tilde{R}_j\tilde{x}_0 + \tilde{v}_j)]}{2}\right) \Sigma_t^{-1}(\tilde{R}_j\tilde{x}_0 + \tilde{v}_j - \tilde{x}_t)}{p(\tilde{x}_t|\tilde{x}_0)} \\ &= \frac{\sum_{\{R_j, v_j\} \in G} \exp\left(\frac{-[B(x_t - (R_jx_0 + v_j))]^T \Sigma_t^{-1} [B(x_t - (R_jx_0 + v_j))]}{2}\right) \Sigma_t^{-1} B(R_jx_0 + v_j - x_t)}{\sum_{\{R_i, v_i\} \in G} \exp\left(\frac{-[B(x_t - (R_ix_0 + v_i))]^T \Sigma_t^{-1} [B(x_t - (R_ix_0 + v_i))]}{2}\right)}. \end{aligned}$$

Finally, we transform the score back to fractional space as $B^{-1}\nabla_{\tilde{x}_t} \log p(\tilde{x}_t|\tilde{x}_0)$.

Using the equivariance property, i.e., $\nabla_{\tilde{x}_t} \log p(\tilde{R}\tilde{x}_t + \tilde{v}|\tilde{x}_0) = \tilde{R}\nabla_{\tilde{x}_t} \log p(\tilde{x}_t|\tilde{x}_0)$, and defining the induced action of $g = \{R, v\}$ on the fractional score as

$$\begin{aligned} \phi(g \cdot x_t|x_0) &\equiv B^{-1}\nabla_{Bx_t} \log p(B(g \cdot x_t)|Bx_0) \\ &= B^{-1}\nabla_{Bx_t} \log p(B(Rx_t + v)|Bx_0) \\ &= B^{-1}\nabla_{Bx_t} \log p(\tilde{R}x_t + \tilde{v}|Bx_0), \end{aligned}$$

we see

$$\begin{aligned} B^{-1}\nabla_{\tilde{x}_t} \log p(\tilde{R}\tilde{x}_t + \tilde{v}|\tilde{x}_0) &= B^{-1}\tilde{R}\nabla_{\tilde{x}_t} \log p(\tilde{x}_t|\tilde{x}_0) \\ &= RB^{-1}\nabla_{\tilde{x}_t} \log p(\tilde{x}_t|\tilde{x}_0) \\ \implies \phi(g \cdot x_t|x_0) &= R\phi(x_t|x_0), \end{aligned}$$

showing $\phi(\cdot)$ has the same desired equivariance behavior as GWN scores for non-hexagonal groups and symmetrized functions $f(\cdot)$ (Eq. 1) that Mirramezani et al. (2025) showed satisfies $f(g \cdot x) = Rf(x)$.

7.10 DIFFUSION TRAINING AND INFERENCE

We followed prior crystal diffusion models (Jiao et al., 2023; 2024; Chang et al., 2025; Zeni et al., 2025) and used a variance-exploding log-uniform noise scheduler $\log \sigma_t \sim \mathcal{U}(\log \sigma_0, \log \sigma_T)$, predictor-corrector stochastic sampling (Song et al., 2021) with a signal-to-noise ratio of 0.4, $T = 1000$ diffusion steps, and $\sigma_{0,xy} = \sigma_{0,z} = 0.002$. For periodic coordinates, we set $\sigma_{T,x_{\text{periodic}}} = 0.5$. For aperiodic coordinates, we set $\sigma_{T,x_{\text{aperiodic}}} = 67.0$ for BiDB and $\sigma_{T,x_{\text{aperiodic}}} = 45.0$ for 2DMatPedia, C2DB, and Alex2D.

We trained with the score matching loss,

$$
\begin{aligned}
L_X = \mathbb{E}_{x_t \sim p(x_t|x_0,W), x_0 \sim p_{\text{data}}, t \sim \mathcal{U}(0,T)} \big[& \\
& \omega_{\text{periodic}} || s_\theta(x_t, t) \odot \mathbb{1}_{\text{periodic}} - \lambda_t \nabla_{x_t} \log p(x_t|x_0) \odot \mathbb{1}_{\text{periodic}} ||_2^2 \\
& + \omega_{\text{aperiodic}} || s_\theta(x_t, t) \odot \mathbb{1}_{\text{aperiodic}} - \sigma_{t,z} \nabla_{x_t} \log p(x_t|x_0) \odot \mathbb{1}_{\text{aperiodic}} ||_2^2 \\
\big], &
\end{aligned}
$$

where $\odot$ is elementwise multiplication, $\mathbb{1}_{\text{aperiodic}} = \mathbf{1} - \mathbb{1}_{\text{periodic}} \in \mathbb{Z}_2^3$ is 1 for aperiodic dimensions and 0 for periodic ones, and loss weight $\lambda_t = \mathbb{E}_{x_t \sim p(x_t|x_0), x_0 \sim p_{w,\text{prior}}} [|| \nabla_{x_t} \log p(x_t|x_0) \odot \mathbb{1}_{\text{periodic}} ||]^{-1} \in \mathbb{R}$. We set $\omega_{\text{periodic}} = 2$ and $\omega_{\text{aperiodic}} = 1$ in our experiments.

Noisy samples x_t were created by sampling Gaussian noise $\epsilon \sim \mathcal{N}(0, I)$ and reparameterizing as $x_t = x_0 + \mathcal{P}_w(\sigma_t \epsilon)$ where $\mathcal{P}_w(\cdot)$ is an orthogonal projection to the tangent space of the Wyckoff position w of x_0. We set $p_{w,\text{prior}}$ to uniform $\mathcal{U}[0,1] \cap w$ for periodic coordinates and Gaussian $\mathcal{N}(0, \sigma_{t,z}^2)$ for aperiodic coordinates.

To construct the uniform distribution over Wyckoff sites $\mathcal{U}[0,1] \cap w$, we sampled uniformly on the Wyckoff shapes. Specifically, we sampled a point for 0D Wyckoff positions. For 1D Wyckoff positions, we sampled a line segment proportionally to its length and then uniformly in the segment. For 2D Wyckoff positions, we pre-computed Delaunay triangulations of the polygonal facets belonging to the Wyckoff position, sampled a triangle proportionally to its surface area, and then sampled in the triangle with a uniform Dirichlet distribution. Coordinates in 3D Wyckoff positions were sampled with rejection sampling from a bounding box around the ASU.

Loss weights for periodic coordinates were approximated with Monte Carlo sampling with s samples as

$$
\lambda_t \approx \Big[\frac{1}{s} \sum_{i=1}^{s} \nabla_{x_t^i} \log p(x_t^i | x_0^i; G, w, \Sigma_t) \Big]^{-1}
$$

In our experiments, we set $s = 2500$. Since crystallographic groups consist of an infinite number of lattice translations, we cannot compute the score of the wrapped normal explicitly. Instead, following prior work (Jiao et al., 2023; 2024), we approximated it with a truncated sum over lattice translations as

$$
\begin{aligned}
& q(x_t|x_0) \propto \\
& \sum_{t_L \in \mathbb{Z}^d \cap [-m,m]^d} \sum_{\{R_j, v_j\} \in G/T_L} \exp \Big[\frac{-1}{2} (x_t - R_j x_0 - v_j - t_L)^T \Sigma_t^{-1} (x_t - R_j x_0 - v_j - t_L)) \Big]
\end{aligned}
$$

where $d = 2$ for layer groups and 3 for space groups. We used $m = 3$.

7.11 MODEL ARCHITECTURE

7.11.1 WYCKOFF-ELEMENT TRANSFORMER

We employed the transformer architecture in SGEquiDiff but leveraged our layer group and Wyckoff position embeddings (Sec. 7.8.1):

$$
\begin{aligned}
z^0 &\leftarrow \mathrm{MLP}(e_G||e_W||e_A) \\
z^{l+1} &\leftarrow \mathrm{EncoderLayer}(z_i^l, m_{\mathrm{causal}}) \\
z_W, z_A &\leftarrow \mathrm{Split}(z^{l_{\max}}) \\
z_A &\leftarrow \mathrm{MLP}(z_A, e_W) \\
p_{W,\mathrm{stop}} &\leftarrow \mathrm{MultiheadDotProductAttentionScore}(K = [e_W^{\mathrm{all}}||e_{\mathrm{stop}}], Q = z_W, \mathrm{mask} = m_W) \\
p_A &\leftarrow \mathrm{MultiheadDotProductAttentionScore}(K = e_A^{\mathrm{all}}, Q = z_A, \mathrm{mask} = m_A)
\end{aligned}
$$

where e_G, e_W, and e_A are embeddings of the crystal's space or layer group, occupied Wyckoff positions, and atomic elements, respectively; $l_{\max}$ is the number of encoder layers; m_{causal} is a causal attention mask enforcing atom orderings; e_W^{all}, e_{stop}, and e_A^{all} are predicted embeddings of all sampleable Wyckoff positions, the stop token, and all sampleable elements, respectively; m_W and m_A are attention masks enforcing lexicographic atom orderings; $p_{W,\mathrm{stop}}$ and p_A are model probabilities over Wyckoff positions, the stop token, and elements; and $\mathrm{EncoderLayer(x, m)}$ is summarized by the following:

$$
\begin{aligned}
x_{\mathrm{norm}} &\leftarrow \mathrm{LN}(x) \\
x &\leftarrow x + \mathrm{MultiheadSelfAttention}(x_{\mathrm{norm}}, m) \\
x &\leftarrow \mathrm{Dropout}(x) \\
x &\leftarrow \mathrm{Dropout}\big(x + \mathrm{Linear}(\mathrm{Dropout}(\mathrm{MLP}(x)))\big)
\end{aligned}
$$

7.11.2 GRAPH NEURAL NETWORK

We modified the FAENet-inspired GNN (Duval et al., 2023) from SGEquiDiff (Chang et al., 2025) to be configurably invariant to either P1 space or layer groups such that it can be symmetrized to any space or layer group with Eq. 1. We used fully-connected graphs in the conventional unit cell with edge features based on relative positions in fractional coordinates (where aperiodic fractional coordinates are scaled to unit variance for stability) and distances in real space. For the real space distances, we used the minimum image convention, where images were masked out from the aperiodic dimension for layer groups:

$$
r_{ij} = \min_j r(x_i, x_j + n_1 e_1 + ... + n_d e_d).
$$

Here, x_i is in fractional coordinates, $n_i \in \mathbb{Z}$, $e_i \in \mathbb{Z}^3$ is an integer lattice translation, $d \in [2, 3]$ indicates how many periodic dimensions there are, and $r(\cdot, \cdot)$ is the distance function.

To embed (relative) positions in fractional coordinates, we used Fourier features. For periodic coordinates, we sampled n_{freq} integer frequencies $\nu_{k,\mathrm{periodic}} \in \mathbb{Z}^3 \cap [-512, 512]^3 \setminus \mathbf{0}$ without replacement with probabilities drawn from a discretized standard normal distribution. For aperiodic coordinates, we sampled n_{freq} random frequencies $\nu_{k,\mathrm{aperiodic}} \sim \mathcal{N}(0, 1) \in \mathbb{R}$. The architecture is

summarized as follows:

$$
\begin{aligned}
x_i &\leftarrow (x_i \bmod 1) \odot \mathbb{1}_{\text{periodic}} + (x_i - \frac{1}{N}\sum_{i=1}^{N} x_i) \odot \mathbb{1}_{\text{aperiodic}} \\
t_{\text{emb}} &= \text{MLP}(c_{\text{noise}}(\text{diag}(\Sigma_t))) \\
e_d &= \text{MLP}(\mathbb{1}_{\text{Crystal has space group symmetry}}) \\
h_i^0 &\leftarrow \text{MLP}\big(e_{a_i} || \text{FourierEmbedding}(x_i, \Sigma_{t,33}) || t_{\text{emb}} || e_d\big) \\
e_{ij} &\leftarrow \text{MLP}\big(\text{FourierEmbedding}(\mathrm{x_j - x_i}, \Sigma_{\mathrm{t,33}}) || \text{RBF}(\mathrm{r_{ij}}) || \text{Norm}(\mathbf{l}) || \mathrm{e_d}\big) \\
f_{ij}^l &\leftarrow \text{MLP}\big(e_{ij} || h_i^l || h_j^l\big) \\
h_i^{l+1} &\leftarrow h_i^l + a \cdot \text{MLP} \circ \text{GraphNorm}\left(\frac{1}{\sqrt{|\mathcal{N}_\mathrm{i}|}} \sum_{\mathrm{j} \in \mathcal{N}_\mathrm{i}} \mathrm{h_j^l} \odot \mathrm{f_{ij}^l}\right) \\
h_i^{l_{\max}} &\leftarrow \text{MLP}(h_i^0 || ... || h_i^{l_{\max}}) \\
\hat{f}_i &\leftarrow \text{MLP}(h_i^{l_{\max}})
\end{aligned}
$$

where

$$
\begin{aligned}
c_{\text{noise}}(\cdot) &= \frac{1}{4}\log(\cdot) \\
c_{\text{in}}(\cdot) &= 1/\sqrt{(\cdot)^2 + \sigma_{z,\text{data}}^2}
\end{aligned}
$$

$$
\begin{aligned}
&\text{FourierEmbedding}(\mathrm{x} \in \mathbb{R}^3, \sigma_{\mathrm{t,z}}) \leftarrow \big[\\
&\quad \mathbb{1}_{\text{crystal is diperiodic}} || c_{\text{in}}(\sigma_{t,z}) x_z \mathbb{1}_{\text{crystal is diperiodic}} || \big(\cos(2\pi x^T w_i) || \sin(2\pi x^T w_i) \big)_{i=0,\ldots,n_{\text{freq}}} \\
&\quad \big] \\
&\quad w_i = 2\pi \cdot \begin{cases} \nu_{i,\text{periodic}} & \text{if } d = 3 \\ (\nu_{i,\text{periodic}}[:2] || \nu_{i,\text{aperiodic}}) & \text{otherwise} \end{cases} \in \mathbb{R}^3.
\end{aligned}
$$

Here, N is the number of atoms in the conventional unit cell, $\mathbb{1}_{\text{periodic}} \in \mathbb{Z}_2^3$ is an indicator vector that is 1 for periodic coordinates and 0 for aperiodic ones, $\mathcal{N}_i$ are the neighbors of atom i, a is a learnable scalar initialized at zero, $\text{RBF}(d_{ij})$ featurizes Cartesian distances in log space using a basis of 50 Gaussians with means from a log-uniform grid between $\log(10^{-6})$ and $\log(\sigma_{T,z})$, $\mathbf{l} = (a, b, c, \alpha, \beta, \gamma)$ are the conventional unit cell lattice parameters where we masked $c = -1$ for layer group symmetric crystals, $\text{Norm}(\cdot)$ applies min-max normalization, GraphNorm (Cai et al., 2020) applies featurewise Z-score normalization over nodes with learnable shift and scaling parameters, $\sigma_{z,\text{data}}^2$ is the dataset variance over aperiodic fractional coordinates, and c_{noise} and c_{in} are employed for training stability (Karras et al., 2022).

We see that $\hat{f}_i$ is invariant to lattice translations because its spatial inputs are minimum-image Cartesian distances under periodic boundary conditions and fractional coordinates with periodic dimensions featurized by plane waves.

7.12 Model hyperparameters

Our model was trained with the Adam optimizer (Kingma & Ba, 2015) on a single NVIDIA A40 GPU. Single-task training on the largest diperiodic materials dataset (Alex2D) took approximately 9 hours. Model evaluation on each dataset took 1-2 hours with a single A40 GPU and 20 CPU cores. Hyperparameters were tuned by manually. The lattice sampler, Wyckoff-element transformer, and diffusion model were trained simultaneously but independently. Early stopping based on validation loss was applied on a per-module basis.

7.13 Dataset details

2DMatPedia and Alexandria are released under the CC BY 4.0 license. C2DB and BiDB are released under the CC BY-NC 4.0 license. For full details on each dataset's DFT settings, please refer to the corresponding papers. Here, we briefly summarize them:

Hyperparameter	Value
Batch size	256
Number of epochs	2000
Lattice length noise range	0.3
Lattice angle noise range	5.0
Lattice sampler hidden dimension	256
Lattice length Fourier scale	5.0
Lattice angle Fourier scale	1.0
Lattice length bin edges Fourier scale	2.0
Lattice angle bin edges Fourier scale	1.0
Lattice parameter embedding dimension	32
Lattice sampler number of hidden layers	3
Transformer dropout rate	0.1
Transformer hidden dimension	256
Transformer number of hidden layers	4
Transformer number of heads	2
GWN lattice translations	3
GWN Monte Carlo samples	2500
Time embedding dimension	128
Number of plane wave frequencies	96
Number of Cartesian distance radial basis functions	96
Edge embedder hidden dimension	128
Node embedder hidden dimension	256
Number of message passing steps	5
Lattice learning rate	1×10^{-4}
Transformer learning rate	1×10^{-4}
GNN learning rate	1×10^{-3}
Weight decay	0.0
Learning rate scheduler	None
Gradient clipping by value	0.5
Joint Alex2D/MP20 training - Alex2D sampling weight	1.3
Joint Alex2D/MP20 training - MP20 sampling weight	1.0

- 2DMatPedia (Zhou et al., 2019): VASP vdW-optB88 functional with the Materials Project's +U corrections (Jain et al., 2013), 520 eV plane wave cutoff, spin polarization, 1e-4 eV ionic convergence, Materials Project k-point densities, 20Å vacuum
- C2DB (Haastrup et al., 2018): GPAW PBE functional, 800 eV plane wave cutoff, 0.01 eV/Angstrom force convergence, 6Å^{-1} k-point densities, 15Å vacuum, 0.05 eV Fermi smearing
- BiDB (Pakdel et al., 2024): GPAW PBE-D3 with custom +U corrections, 800 eV plane wave cutoffs, spin polarization, 12Å^{-1} k-point densities, 15Å vacuum, 50 meV Fermi-Dirac smearing
- Alexandria (Schmidt et al., 2024): VASP v5.2 PBE+U, 520 eV cutoff, 5×10^{-3} eV/A force convergence, 15Å vacuum

7.13.1 Layer centering and monolayer isolation from bilayers

Since raw structures from 2DMatPedia, C2DB, BiDB, and Alexandria were represented with a bounded 3D periodic unit cell, the superficial periodic boundaries along the aperiodic c-axis often "cut" layers. To make atoms always appear contiguously, we checked consecutive differences in each atom position's fractional z coordinate. If the largest difference was >7Å, we determined that vacuum was found in the middle of the cell (and thus the layer was erroneously cut by the periodic boundary) and translated all atoms along the c-axis until they wrapped contiguously to the bottom of the cell. The atoms were then translated to $z = 0.5$.

Similarly, to isolate monolayers from bilayers for computing binding energies and interlayer distances, we found the largest gap in consecutive z-coordinates. All atoms above and below the gap were classified as belonging to the upper and lower monolayer, respectively.

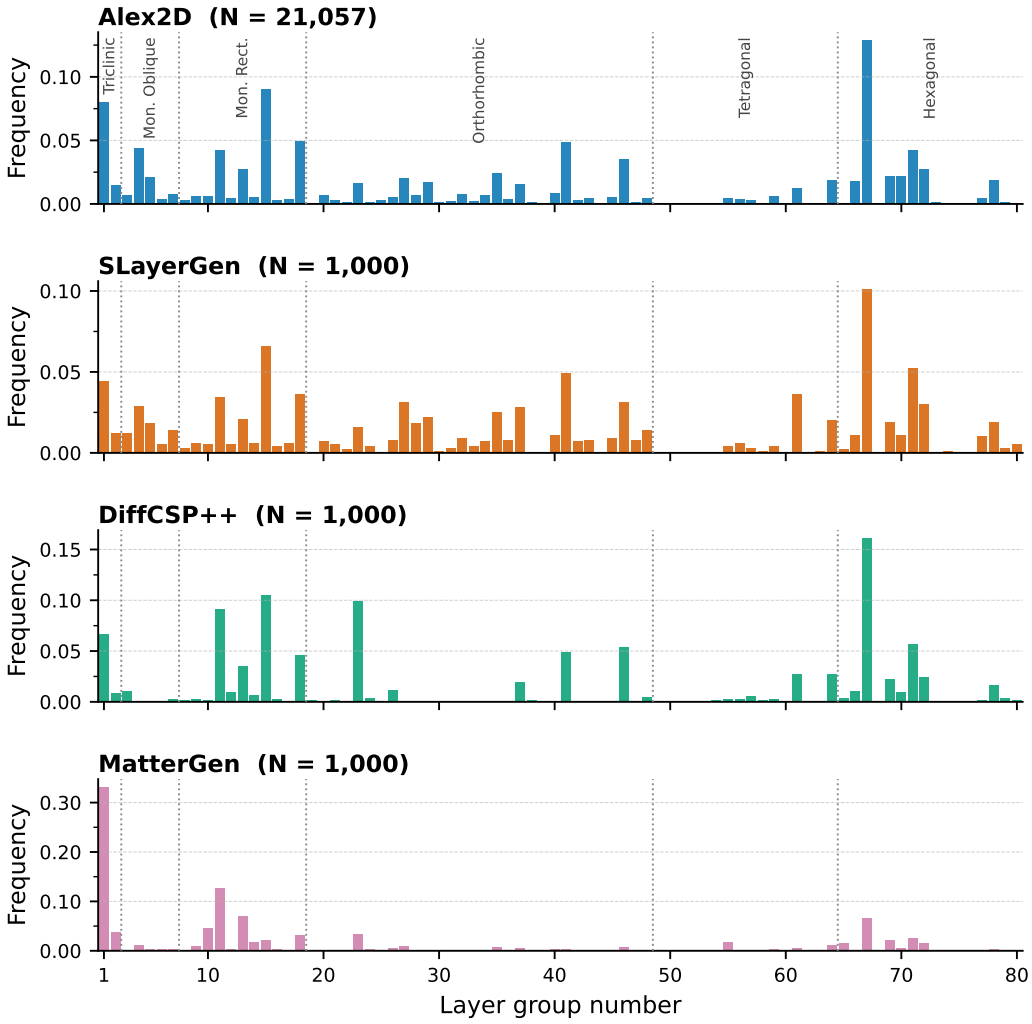


Figure 5: Histograms of occupied layer groups by samples from generative models and by their training data from Alexandria (Schmidt et al., 2024; Wang et al., 2023). Layer groups were determined by the `get_layergroup` function in `spglib` (Fu et al., 2024a; Togo et al., 2024) using tolerances of 0.01Å for ground-truth DFT-relaxed structures and 0.1Å for samples from generative models. Vertical dashed lines separate layer groups by crystal system. We observe that SLayerGen preserves the layer group distribution of the training set, DiffCSP++ undersamples many orthorhombic and monoclinic groups, and MatterGen heavily oversamples low symmetry P1 crystals.

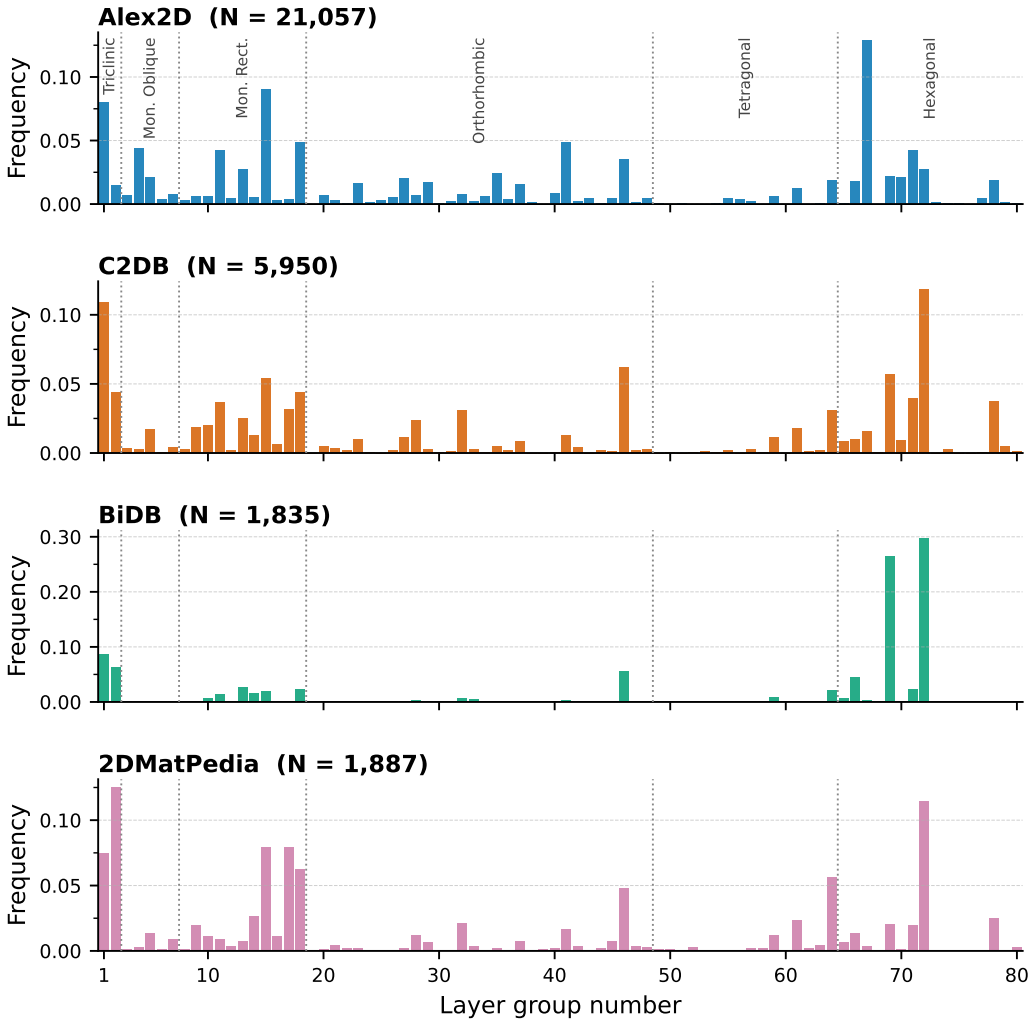


Figure 6: Histograms of occupied layer groups by our filtered training data from Alexandria (Schmidt et al., 2024; Wang et al., 2023), C2DB (Haastrup et al., 2018), BiDB (Pakdel et al., 2024), and 2DMatPedia (Zhou et al., 2019). Layer groups were determined by the `get_layergroup` function in `spglib` (Fu et al., 2024a; Togo et al., 2024) using tolerances of 0.01Å. Vertical dashed lines separate layer groups by crystal system.